

Low-order models for predicting radiative transfer effects on Rayleigh–Bénard convection in a cubic cell at different Rayleigh numbers

Laurent Soucasse^{1,†}, Bérengère Podvin², Philippe Rivière¹
and Anouar Soufiani¹

¹Laboratoire EM2C, CNRS, CentraleSupélec, Université Paris-Saclay, 8-10 rue Joliot Curie, 91192 Gif-sur-Yvette, France

²LISN, CNRS, Université Paris-Saclay, Bât 507, rue du Belvédère, Campus Universitaire, 91405 Orsay, France

(Received 6 October 2020; revised 4 February 2021; accepted 18 March 2021)

This paper presents low-order models of Rayleigh–Bénard convection of a radiating gas in a cubic cell, in the Rayleigh number range $Ra \in [10^6–10^8]$. Numerical simulations are carried out for an air–H₂O–CO₂ mixture assumed to be radiating (coupled case) or transparent (uncoupled case). When coupling with radiation, it is shown that the kinetic energy of the flow and the thermal energy increase. At $Ra = 10^6$, planar flow states are observed when radiation is taken into account, while diagonal flow states prevail in the uncoupled case. From $Ra \geq 3 \times 10^7$, quasi-stable diagonal flows are observed in both coupled and uncoupled simulations, with occasional brief reorientations. The reorientation frequency seems to decrease with the Rayleigh number and seems to increase with radiation. A proper orthogonal decomposition (POD) analysis reveals that 11 of the first 12 POD eigenfunctions are preserved over the Rayleigh number range, whatever the coupling conditions. However, POD eigenvalues are higher with radiation. POD-based low-order models are derived at different Rayleigh numbers, for both coupled and uncoupled cases. Radiative transfer effects are added in the model in an *a priori* fashion, from uncoupled simulation data. Coupled POD models predict the energy increase with radiation and the loss of stability of the diagonal rolls at $Ra = 10^6$. Uncoupled and coupled models correctly reproduce reorientation frequencies over the Rayleigh number range. Finally, a generalised model is derived, solely based on uncoupled simulation data at $Ra = 10^7$ and energy scaling laws. This generalised model captures the change in dynamics associated with radiation effects and variations in Rayleigh number, except at $Ra = 10^6$.

Key words: Bénard convection, low-dimensional models

† Email address for correspondence: laurent.soucasse@centralesupelec.fr

1. Introduction

The problem of Rayleigh–Bénard convection (RBC) consists of a fluid layer confined between two horizontal plates, heated from below and cooled from above. This problem has been widely studied to model buoyancy-driven flows encountered in geophysics or engineering, and to understand the fundamental properties of turbulence. In the turbulent regime, the complexity comes from the chaotic nature of the flow and the wide range of time and length scales on which velocity and temperature fields vary.

The dynamics of turbulent RBC becomes more complicated when the working fluid is a radiating gas, which emits and absorbs thermal radiation. It is the case, for instance, in the atmosphere or in confined environments such as buildings, where the fluid (the air) contains radiating molecules in the infrared such as water vapour or carbon dioxide. Radiative transfer effects on turbulent convection were first investigated by Spiegel (1957), who showed that radiation acts as a dissipation mechanism of temperature fluctuations. This damping effect prevails over conductive dissipation for large and intermediate turbulent scales and vanishes for small turbulent scales from a critical length scale depending on the radiative properties of the medium (Soufiani 1991). However, in the case of thermally driven flow, radiation also affects the mean temperature gradient and buoyant motion. Several researchers have reported an increase of the mean kinetic energy of the flow due to an increase of the mean potential energy in various configurations involving a radiating gas: in a differentially heated cavity (Kogawa *et al.* 2017), in a Rayleigh–Bénard cavity (Soucasse, Rivière & Soufiani 2014a) or for a confined plume generated by a linear heat source (Wang *et al.* 2020). The cost of radiative transfer computations in a turbulent medium restricts the numerical investigation of radiation effects due to the angular, spectral and spatial dependence of the radiation field. Experimental works are also challenging to undertake, as non-intrusive techniques that do not perturb the radiation field are required. Therefore, the question arises whether a low-order model could capture radiation effects on RBC, given that radiative transfer rather affects the large and intermediate scales of the flow.

In the case of a non-radiating gas, the large-scale motion in RBC, also referred to as large-scale circulation (LSC), has aroused a great interest as it intermittently changes orientation. In cylindrical cells with aspect ratio of unity (diameter equal to height), azimuthal rotation of the LSC and reversal of the LSC (sudden change of direction in the same circulation plane) have been reported by experimental studies (Sreenivasan, Bershadski & Niemela 2002; Brown, Nikolaenko & Ahlers 2005) and numerical studies (Benzi & Verzicco 2008; Mishra *et al.* 2011). In cubic cells, low-frequency reorientations of the LSC have been observed between four quasi-stable states, corresponding to the LSC lying in the two diagonal vertical planes of the cube associated with clockwise and anticlockwise motion (Vasiliev *et al.* 2016; Foroozani *et al.* 2017). For both cylindrical and rectangular cells, it has been shown that the LSC dynamics is very sensitive to the aspect ratio (Xi & Xia 2008; Vasiliev & Frick 2011; Ni, Huang & Xia 2015).

Several models have been proposed to explain the LSC dynamics in RBC for non-radiating gases. Brown & Ahlers (2007, 2008) derived a stochastic two-equation model to predict the time evolution of the strength and the azimuthal orientation of the LSC in cylindrical geometries. This model has been extended for cubical geometries, by the addition of a potential term which drives the azimuthal angle towards the vertical edges of the cube and the LSC in the diagonal planes (Bai, Ji & Brown 2016; Ji & Brown 2020). Another phenomenological model for reversals in a square cell has been proposed by Araujo, Grossmann & Lohse (2005). From this model, the authors have established a range of Prandtl and Rayleigh numbers where reversals occur and a scaling law for the reversal frequency. Other modelling approaches rely on modal decomposition of temperature

and velocity fields based on Fourier modes (Chandra & Verma 2011), Koopman modes (Giannakis *et al.* 2018) or proper orthogonal decomposition (POD) modes (Bailon-Cuba, Emran & Schumacher 2010; Podvin & Sargent 2012).

Proper orthogonal decomposition is often used in fluid mechanics to extract large-scale coherent structures from numerical or experimental data. The POD modes form an orthogonal basis, which is optimal to represent the flow regarding its energy content. A low-order model for the flow can be easily derived from a Galerkin projection of the Navier–Stokes equation onto the orthogonal POD basis. In a previous study we have developed a POD model for capturing reorientations of the LSC in a cubic Rayleigh–Bénard cell at a Rayleigh number $Ra = 10^7$ (Soucasse *et al.* 2019). In the presence of radiating species, we have shown that radiation effects can be taken into account by a POD model, from a rigorous projection of the radiative source term of the energy balance onto the POD basis (Soucasse *et al.* 2020). However, a frequent pitfall of POD models is that their prediction capabilities are restricted in the neighbourhood of the flow parameters associated with the data. This paper aims to examine at which extent radiative transfer effects can be predicted from uncoupled simulation data across a wide range of Rayleigh numbers in a cubic cell. Direct numerical simulations (DNS), coupled or uncoupled with radiation, have been performed in the range $Ra \in [10^6-10^8]$, where reorientations are more likely to be observed (Sugiyama *et al.* 2010). A radiating air–H₂O–CO₂ mixture at room temperature has been considered to make our study relevant for building applications. Numerical simulations are presented in § 2 and associated POD analysis is performed in § 3. Uncoupled POD models (non-radiating case) and predicted coupled POD models (radiating case) are derived in §§ 4 and 5 at different Rayleigh numbers. Finally, a general model across the Rayleigh range, solely based on uncoupled simulation data at $Ra = 10^7$ and energy scaling laws, is developed in § 6.

2. DNS

2.1. Problem set-up

We consider the natural convection flow of an air–H₂O–CO₂ mixture confined in a cubic Rayleigh–Bénard cell, with top and bottom isothermal walls at T_{cold} and T_{hot} and adiabatic vertical walls. The six walls are characterised by uniform grey emissivities ε , the horizontal isothermal walls being black ($\varepsilon = 1$) and the vertical adiabatic walls being perfectly diffuse reflecting ($\varepsilon = 0$). The parameter controlling the flow regime is the Rayleigh number defined by

$$Ra = \frac{g\beta\Delta TL^3}{\nu_f a}, \quad (2.1)$$

where g is the gravitational acceleration, $\beta = 1/T_0$ is the thermal expansion coefficient (T_0 being the mean temperature), L is the size of the cavity, ν_f is the kinematic viscosity, a is the thermal diffusivity and $\Delta T = T_{hot} - T_{cold}$ is the temperature difference between hot and cold walls. We investigate the Rayleigh range $Ra \in [10^6-10^8]$ in which reorientations are likely to be observed (Sugiyama *et al.* 2010). We vary the Rayleigh number by changing the temperature difference ΔT and other parameters are fixed. In order to make our study relevant for building applications, we consider an air–H₂O–CO₂ mixture at a mean temperature of $T_0 = 300$ K, of molar composition $X_{H_2O} = 0.02$ and $X_{CO_2} = 0.001$, and the cavity size is set to $L = 1$ m, so that the temperature difference vary in the range $\Delta T \in [1.1 \times 10^{-2}-1.1]$ K. Thermophysical properties are assumed to be uniform (low temperature differences), not affected by the small amount of water

vapour and carbon dioxide, and constant at all Rayleigh numbers (thermal conductivity $\lambda = 0.0263 \text{ W m}^{-1} \text{ K}^{-1}$, thermal diffusivity $a = 2.25 \times 10^{-5} \text{ m}^2 \text{ s}^{-1}$, Prandtl number $Pr = \nu_f/a = 0.707$).

Mass, momentum and energy balance are made dimensionless using the cavity size L , the reference time $L^2/(a\sqrt{Ra})$ and the reduced temperature $\theta = (T - T_0)/\Delta T$ and write under Boussinesq approximation as

$$\nabla \cdot \mathbf{u} = 0, \tag{2.2}$$

$$\frac{\partial \mathbf{u}}{\partial t} + \mathbf{u} \cdot \nabla \mathbf{u} = -\nabla p + Pr\theta \mathbf{e}_z + \frac{Pr}{\sqrt{Ra}} \nabla^2 \mathbf{u}, \tag{2.3}$$

$$\frac{\partial \theta}{\partial t} + \mathbf{u} \cdot \nabla \theta = \frac{1}{\sqrt{Ra}} \left(\nabla^2 \theta + \mathcal{P}^{rad} \right), \tag{2.4}$$

where $\mathbf{u} = (u, v, w)$ is the dimensionless velocity vector and p the dimensionless motion pressure. The velocity is zero on all walls. The temperature is set to 0.5 and -0.5 , respectively, on the bottom and top walls. The conductive flux $-\nabla \theta \cdot \mathbf{n}$ is zero on the four lateral walls, as these walls have a zero radiative emissivity.

The dimensionless radiative power \mathcal{P}^{rad} in (2.4) accounts for absorption and emission of thermal radiation by the medium and is defined by

$$\mathcal{P}^{rad}(\mathbf{r}) = \frac{L^2}{\lambda \Delta T} \int_{\nu} \kappa_{\nu} \left(\int_{4\pi} I_{\nu}(\boldsymbol{\Omega}, \mathbf{r}) \, d\boldsymbol{\Omega} - 4\pi I_{\nu}^{\circ}(T(\mathbf{r})) \right) \, d\nu, \tag{2.5}$$

where $I_{\nu}(\boldsymbol{\Omega}, \mathbf{r})$ is the actual radiative intensity at frequency ν , direction $\boldsymbol{\Omega}$ and position \mathbf{r} . $I_{\nu}^{\circ}(T(\mathbf{r}))$ is the Planck equilibrium intensity at temperature T and κ_{ν} is the absorption coefficient of the medium. In accordance with the Boussinesq approximation, the absorption coefficient is assumed to be spatially uniform. The Planck equilibrium intensity is given by

$$I_{\nu}^{\circ}(T(\mathbf{r})) = \frac{2h\nu^3}{c_0^2} \frac{1}{\exp\left(\frac{h\nu}{k_B T(\mathbf{r})}\right) - 1}, \tag{2.6}$$

where h is the Planck constant, k_B is the Boltzmann constant and c_0 the speed of light in vacuum. The radiative intensity field is obtained by solving the radiative transfer equation

$$\boldsymbol{\Omega} \cdot \nabla I_{\nu}(\boldsymbol{\Omega}, \mathbf{r}) = \kappa_{\nu} \left(I_{\nu}^{\circ}(T(\mathbf{r})) - I_{\nu}(\boldsymbol{\Omega}, \mathbf{r}) \right). \tag{2.7}$$

The associated boundary condition at boundary points \mathbf{r}^w for grey diffuse reflecting walls writes as

$$I_{\nu}(\boldsymbol{\Omega}, \mathbf{r}^w) = \varepsilon I_{\nu}^{\circ}(T(\mathbf{r}^w)) + \frac{1 - \varepsilon}{\pi} \int_{\boldsymbol{\Omega}' \cdot \mathbf{n} < 0} I_{\nu}(\boldsymbol{\Omega}', \mathbf{r}^w) |\boldsymbol{\Omega}' \cdot \mathbf{n}| \, d\boldsymbol{\Omega}', \tag{2.8}$$

for directions $\boldsymbol{\Omega}$ such that $\boldsymbol{\Omega} \cdot \mathbf{n} > 0$, \mathbf{n} being the wall normal directed towards the inside of the domain.

It is worth noting that the flow equations are written and solved in dimensionless form, while the radiative transfer equations are treated in dimensional form since we consider an actual molecular radiating gas. A key parameter for radiation is the optical thickness $\tau_{\nu} = \kappa_{\nu} L$ that varies over several orders of magnitude in our model. Considering a grey fluid (wavelength-independent absorption) would facilitate a parametric study of radiation effects but would fail to represent the behaviour of actual radiating gases.

2.2. Numerical methods

The numerical methods used for solving the coupled system of (2.2)–(2.4) and (2.7) are presented and validated in detail by Soucasse, Rivière & Soufiani (2016) and Soucasse *et al.* (2020). We briefly mention here the main features of the coupled algorithm.

Navier–Stokes equations are solved using a Chebyshev collocation method (Xin & Le Quéré 2002). Domain decomposition along the vertical direction is carried out by the Schur complement method to make the computations parallel (Xin, Chergui & Le Quéré 2008). Time integration is performed through a second-order semi-implicit scheme. The velocity divergence-free condition is enforced using a projection method. The radiative transfer equation is solved using a ray-tracing algorithm, made parallel by distributing the rays among the different processors. The 4π angular domain is uniformly discretised using 900 rays from volume cell centres and 450 rays from boundary cell centres. The Absorption distribution function (known as ADF) model (Pierrot *et al.* 1999) is used to take into account the spectral variations of the absorption coefficient of the air–H₂O–CO₂ mixture: it consists in substituting the integration over the frequency with an integration over the values of the absorption coefficient, for which a coarse logarithmic discretisation is sufficient. In the present study, the values of the absorption coefficient have been logarithmically discretised in 16 classes and the accuracy of the model has been shown to be better than 1% (Soucasse *et al.* 2012). Model parameters and computational details for the considered mixture are given by Soucasse (2013) and Soucasse *et al.* (2012).

Direct numerical simulations have been performed, considering the air–H₂O–CO₂ mixture as radiating (coupled case) or transparent (uncoupled case, $X_{H_2O} = 0$, $X_{CO_2} = 0$ and thus $\mathcal{P}^{rad} = 0$). Simulation parameters are given in table 1. Five different Rayleigh numbers have been considered: $Ra = \{10^6; 3 \times 10^6; 10^7; 3 \times 10^7; 10^8\}$. The convection mesh is built from Chebyshev collocation points. We have checked that the number of points in the boundary layers is sufficient regarding the criterion proposed by Shishkina *et al.* (2010). Up to $Ra = 10^7$, the radiation mesh is built from the convection mesh, coarsened by a factor of two in each direction of space. For $Ra = 3 \times 10^7$ and $Ra = 10^8$, the radiation mesh is coarsened by a factor of four in each direction of space compared with the convection mesh and we use a radiation subgrid model (Soucasse, Rivière & Soufiani 2014b) to account for the radiation of small spatial scales. This subgrid model has been validated in various configurations and its accuracy is approximately a few per cent on radiative power and wall fluxes. It has been used for the simulation of coupled natural convection and radiation in a differentially heated cavity at $Ra = 3 \times 10^9$ (Soucasse *et al.* 2016). Finally, an explicit coupling is carried out between flow and radiation calculations and the radiation source term is updated every 10 convection time steps δt (the flow time step is imposed by numerical stability constraints and does not correspond to significant variations of the temperature field). Time integration is carried out over a period Δt once the asymptotic regime (statistically steady) is reached.

It should be mentioned here that radiation calculations are much more computationally expensive than convection calculations (the CPU time is approximately 30 times greater in the coupled case).

2.3. Radiative transfer effects

Radiative transfer effects on RBC at $Ra = 10^7$ have been discussed in a previous work (Soucasse *et al.* 2020). When the fluid emits and absorbs radiation, heat transfer is no longer restricted to the boundary layer region. An energy exchange between convection and radiation in the core of the cavity leads to a significant increase of the convective

Ra	Convection mesh	Radiation mesh	$\delta t \times 10^3$	Δt
10^6	$81 \times 81 \times (4 \times 21)$	$40 \times 40 \times 40$	5	10 000
3×10^6	$81 \times 81 \times (4 \times 21)$	$40 \times 40 \times 40$	2.5	10 000
10^7	$81 \times 81 \times (4 \times 21)$	$40 \times 40 \times 40$	2.5	10 000
3×10^7	$121 \times 121 \times (6 \times 21)$	$30 \times 30 \times 30^a$	$2/1.5^b$	5000
10^8	$161 \times 161 \times (8 \times 21)$	$40 \times 40 \times 40^a$	1	5000

Table 1. Simulation parameters: convection mesh, radiation mesh, convection time step δt and integration time interval Δt in the asymptotic regime. For the convection mesh, numbers in parenthesis indicate the number of spatial domains times the number of collocation points in the vertical in each domain.

^aRadiation subgrid model is used; ^b δt is 2×10^{-3} in the uncoupled simulation and 1.5×10^{-3} in the coupled simulation.

flux compared with the uncoupled case. The LSC is strengthened and both mean and turbulent kinetic energies increase. Temperature fluctuations also increase but to a lesser extent because of radiative damping.

The same effects are observed at other Rayleigh numbers. The total kinetic energy $e_k = \int 0.5 \langle \mathbf{u} \cdot \mathbf{u} \rangle d\mathbf{r}$, the total thermal energy $e_\theta = \int 0.5 \langle \theta\theta \rangle d\mathbf{r}$, the conductive flux at the walls $q_{cond} = \int \langle \partial\theta/\partial z \rangle dx dy$ and the convective flux in the core ($z = 0.5$) $q_{conv} = \sqrt{Ra} \int \langle w\theta \rangle dx dy$ are displayed in figure 1 as a function of the Rayleigh number (where $\langle \cdot \rangle$ denotes the time average). It can be noticed that the kinetic energy and the convective flux significantly increase in the presence of radiation while the thermal energy and the conductive flux are not much affected. However, radiation effects diminish with the Rayleigh number. This can be explained by the following scaling analysis. If the temperature dependence of the Planck equilibrium intensity is linearised around the mean temperature T_0 , an order of magnitude for the dimensional radiative power is $16\kappa_P\sigma T_0^3\Delta T$, where $\kappa_P = \int_V \kappa_\nu I_\nu^\circ(T_0) d\nu \times (\pi/\sigma T_0^4)$ is the Planck mean absorption coefficient of the mixture, σ is the Stefan–Boltzmann constant. Therefore, the radiative source term in the energy balance (2.4) roughly scales as

$$\frac{\mathcal{P}^{rad}}{\sqrt{Ra}} \sim O\left(\frac{1}{\sqrt{Ra}} \frac{16\kappa_P\sigma T_0^3 L^2}{\lambda}\right), \tag{2.9}$$

and decreases in $Ra^{-1/2}$ while the order of magnitude of the convective term $\mathbf{u} \cdot \nabla\theta$ remains constant.

The unsteady dynamics of RBC in a cubic container is characterised by low-frequency reorientations of the LSC (Bai *et al.* 2016; Foroozani *et al.* 2017), that can be monitored using the time evolution of the x and y components of the angular momentum with respect to the cavity centre \mathbf{r}_0 :

$$\mathbf{L} = \int (\mathbf{r} - \mathbf{r}_0) \times \mathbf{u} d\mathbf{r}. \tag{2.10}$$

Figure 2 shows the time evolution of components L_x and L_y at the different Rayleigh numbers for the coupled and uncoupled cases. Note that time integration is shorter for the two highest Rayleigh numbers.

The uncoupled case is characterised at each Rayleigh number by quasi-stable diagonal states, with abrupt reorientations between these states. A diagonal state means that the LSC lies in one of the two diagonal planes $x = y$ or $x = 1 - y$, with clockwise

Low-order models for radiation effects on RB convection

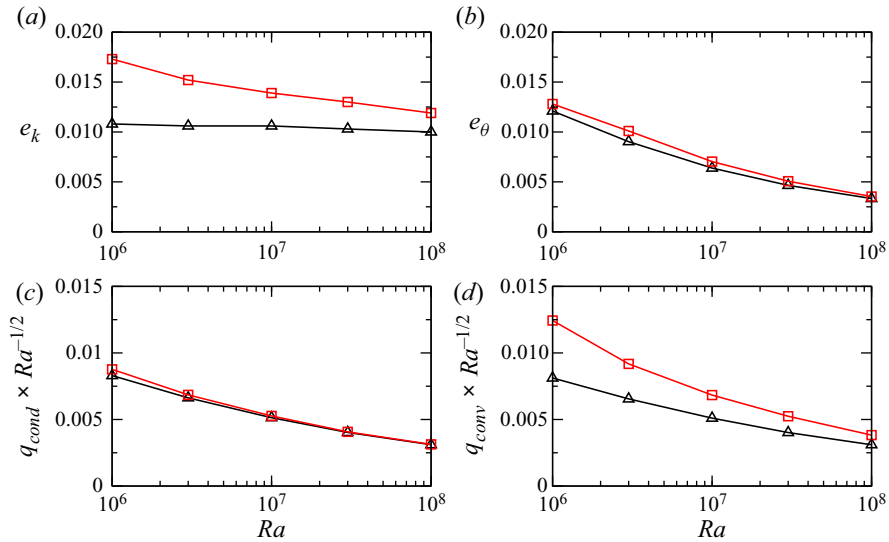


Figure 1. Total kinetic energy e_k , total thermal energy e_θ , conductive flux at the wall q_{cond} and convective flux in the core q_{conv} as a function of the Rayleigh number for coupled (red squares) and uncoupled (black triangles) cases.

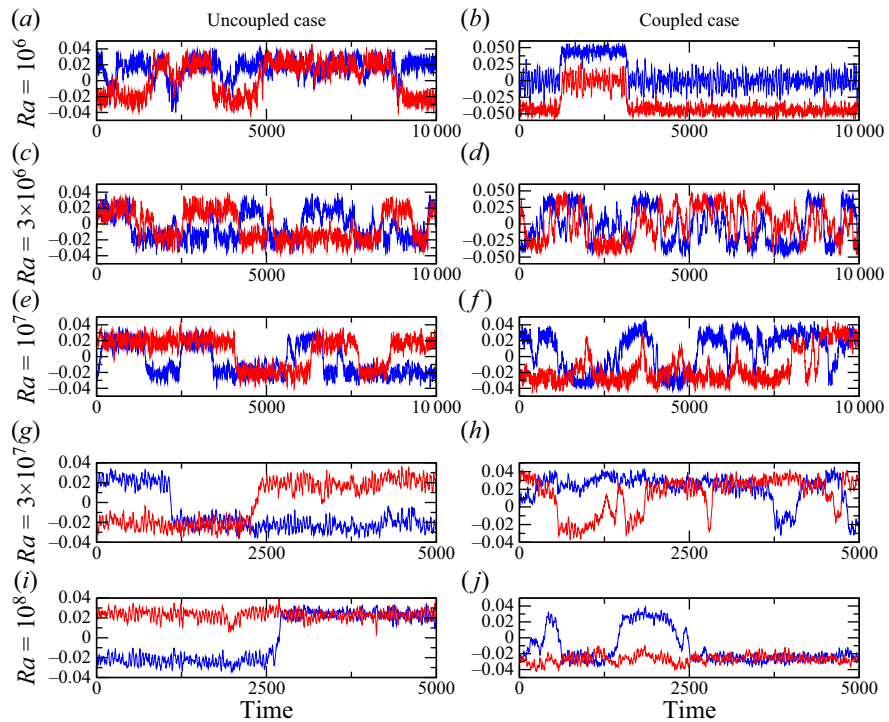


Figure 2. Time evolution of x and y components of angular momentum L_x (blue lines) and L_y (red line).

or anticlockwise motion (four diagonal states are available), and is characterised by a non-zero equilibrium value for both L_x and L_y components. Sudden reorientations between two diagonal states occur when either L_x or L_y changes sign, which corresponds

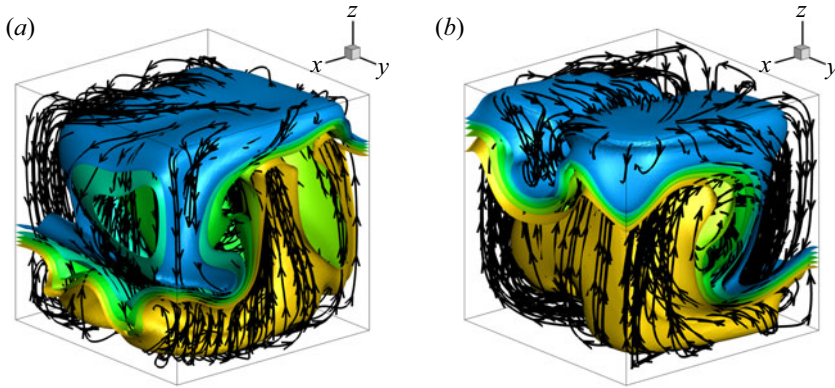


Figure 3. Instantaneous flow field at $Ra = 10^6$ and $t = 5000$ for uncoupled (a) and coupled (b) cases. Streamlines and isotherms $\theta = \{0; \pm 0.05; \pm 0.1\}$. In the uncoupled case (panel (a)) a diagonal state is observed ($L_x > 0, L_y > 0$) while in the coupled case (panel (b)) a planar state is observed ($L_x \simeq 0, L_y < 0$).

to a rotation of $\pi/2$ of the LSC around the vertical axis. A detailed description of the reorientation process in the cubic cell and associated flow patterns is provided by Foroozani *et al.* (2017) and Vasiliev *et al.* (2019). Although the overall dynamics is similar over the Rayleigh number range, it can be noticed that the stability of the diagonal states increases with the Rayleigh number: the flow spends less time around zero angular momentum and reorientations are less frequent when the Rayleigh number increases. At $Ra = 10^6$, the dynamics is more chaotic with quick passing around zero of either L_x or L_y components. At $Ra = 10^8$, the oscillation amplitude of L_x and L_y around the equilibrium value is weaker and only one reorientation event is observed during the sequence (only two of the four diagonal states are visited in this case).

In the coupled case, a significant change in dynamics compared with the uncoupled case is noticeable at $Ra = 10^6$, where quasi-stable planar states are observed. A planar state means that the LSC lies either in x planes or y planes, with clockwise or anticlockwise motion (four planar states are available), and is characterised by a zero equilibrium value for one of the two components L_x or L_y . Figure 3 shows a snapshot of temperature and velocity fields at $Ra = 10^6$. In the uncoupled case (figure 3a) a diagonal state is observed as the LSC lies in the diagonal plane $x = 1 - y$ with $L_x > 0, L_y > 0$. The fluid flows up along the right vertical edge $(x; y) = (0; 1)$ and flows down along the left vertical edge $(x; y) = (1; 0)$. This main diagonal roll is slightly tilted and small counter-rotating rolls are noticeable in the top right corner $(x; y; z) = (0; 1; 1)$ and in the bottom left corner $(x; y; z) = (1; 0; 0)$. In the coupled case (figure 3b) a planar state is observed as the LSC lies in y planes with $L_x \simeq 0, L_y < 0$. The fluid flows up along the front plane $x = 1$ and flows down along the rear plane $x = 0$. Counter-rotating structures are noticeable near the top horizontal edge $(x; z) = (1; 1)$ and the bottom horizontal edge $(x; z) = (0; 0)$. For $Ra \geq 3 \times 10^7$, quasi-stable diagonal states are observed with radiation. However, for a given Rayleigh number, the dynamics is more chaotic and reorientations seem to be more frequent when the flow is coupled with radiation. It is worth noticing here that, although stable planar states are not observed in the uncoupled case, they have been reported at low Rayleigh numbers (Puigjaner *et al.* 2004).

In order to quantify radiative transfer effects on the temporal dynamics we have computed two characteristic frequency scales: the circulation frequency f_c (or circulation time $\tau_c = 1/f_c$) and the reorientation frequency f_r (or reorientation time $\tau_r = 1/f_r$).

Ra	$f_c \times 10^2$		$f_r \times 10^3$	
	Uncoupled	Coupled	Uncoupled	Coupled
10^6	2.12	2.86	1.3 ± 0.3	N/A
3×10^6	2.06	2.47	2.2 ± 0.4	N/A
10^7	2.05	2.33	1.4 ± 0.4	1.7 ± 0.4
3×10^7	2.03	2.27	0.4 ± 0.3	1.3 ± 0.5
10^8	2.03	2.19	N/A	1.1 ± 0.5

Table 2. Circulation frequency f_c and reorientation frequency f_r for the uncoupled and coupled cases at different Rayleigh numbers. The value N/A is indicated when it was not possible to obtain a value (less than two switches observed at $Ra = 10^8$ – uncoupled case, many rapid switches at $Ra = 3 \times 10^6$ – coupled case) or when planar flow states are observed at $Ra = 10^6$ – coupled case.

The circulation frequency is a high frequency associated with the rotation frequency of the LSC roll. Frequencies are reported in table 2. The circulation frequency is estimated using a reference ellipsoid path length in the diagonal plane and a reference velocity. In the uncoupled case, the circulation frequency is nearly constant with the Rayleigh number as convective time units are used. In the coupled case, the increase of the kinetic energy leads to an increase of the circulation frequency. This increase compared with the uncoupled case diminishes with the Rayleigh number. The reorientation frequency is estimated by tracking the zeros of the filtered time evolution of L_x and L_y to avoid small-scale noise. Data in table 2 confirm the observations of figure 2: the reorientation frequency seems to decrease with the Rayleigh number and, at a given Rayleigh number, seems to be higher when radiation is taken into account.

It should be noted here that the uncertainty associated with reorientation frequencies is significant, owing to the few reorientations. If we assume a Poisson distribution of reorientation events (as it has been observed for reversals in cylindrical cells Sreenivasan *et al.* (2002)), the uncertainty on the number of reorientations N_r would be $\pm\sqrt{N_r}$, and the uncertainty on the reorientation frequency f_r would be $\pm\sqrt{(f_r/\Delta t)}$, Δt being the integration time. Uncertainties on reorientation frequencies are given in table 2. Relative uncertainties range from 20 % ($Ra = 3 \times 10^6$, uncoupled case) to 70 % ($Ra = 3 \times 10^7$, uncoupled case). These uncertainties moderate the conclusions on radiative transfer effects on the reorientation frequency, especially at $Ra = 10^7$ where the increase of the reorientation frequency with radiation is not statistically significant. However, the decrease of the reorientation frequency with the Rayleigh number in the uncoupled case seems to be statistically significant in the range $3 \times 10^6 \leq Ra \leq 10^8$ and has been reported in other works (Sugiyama *et al.* 2010).

3. POD

3.1. Methodology

The POD in fluid mechanics aims at finding an optimal basis of spatial eigenfunctions $\phi_n(\mathbf{r})$ to represent an unsteady flow variable vector $\mathbf{U}(\mathbf{r}, t)$ of size M on a low-dimensional subspace. The POD eigenfunctions or POD modes $\phi_n(\mathbf{r})$ are solutions of the following eigenvalue problem (Berkooz, Holmes & Lumley 1993):

$$\int \sum_{k=1}^M \left\langle U^m(\mathbf{r}, t) U^k(\mathbf{r}', t) \right\rangle \phi_n^k(\mathbf{r}') d\mathbf{r}' = \lambda_n \phi_n^m(\mathbf{r}), \quad (3.1)$$

where $\langle \cdot \rangle$ denotes the time average. They form an orthonormal basis allowing the decomposition

$$U(\mathbf{r}, t) = \sum_{n=1}^{\infty} a_n(t) \phi_n(\mathbf{r}), \quad (3.2)$$

where the projection coefficients $a_n(t)$ are statistically uncorrelated and their energy is equal to the eigenvalue such that $\langle a_n(t) a_m(t) \rangle = \delta_{nm} \lambda_n$, where δ_{nm} is the Kronecker symbol. The eigenvalue associated with a POD mode is thus a measure of its energy content and the objective is to restrict the decomposition (3.2) to a few modes with the largest eigenvalues so that the associated low-order subspace captures most of the energy of the field $U(\mathbf{r}, t)$. To take into account the coupling between velocity and temperature fields in thermal convection, we define the flow variable vector as $U = \{\mathbf{u}, \gamma\theta\}$ ($M = 4$), where γ is a rescaling factor

$$\gamma = \sqrt{\left\langle \frac{\int \mathbf{u}(\mathbf{r}, t) \cdot \mathbf{u}(\mathbf{r}, t) \, d\mathbf{r}}{\int \theta^2(\mathbf{r}, t) \, d\mathbf{r}} \right\rangle}, \quad (3.3)$$

such that velocity and temperature fields have the same energy (Podvin & Le Quéré 2001). The POD modes thus combine velocity and temperature: $\phi_n = \{\phi_n^u, \gamma\phi_n^\theta\}$.

Equation (3.1) is solved in practice using the method of snapshots (Sirovich 1987). A snapshot set of 1000 samples $U(\mathbf{r}, t_i)$ is extracted from each simulation at discrete times t_i with a fixed sampling period of 10 dimensionless time units for $10^6 \leq Ra \leq 10^7$ and a fixed sampling period of five dimensionless time units for $3 \times 10^7 \leq Ra \leq 10^8$. This sampling period might seem large compared with the transition time between two states and the few reorientations, but according to Podvin & Sergent (2017), precursor events for reorientations are associated with large-scale interactions during relatively large time scales (of the order of the reorientation period). However, we have seen in the time evolution of the angular momentum components in figure 2 that the four possible quasi-stable flow states (planar or diagonal) were not necessarily visited or not equally represented during the time sequence, although there is no physical evidence suggesting that these states are not equiprobable. This is an artefact owing to the relatively short simulation time compared with the time scale separating two reorientations, especially at high Rayleigh number. In order to enforce an equal statistical weight for each flow state and to improve the convergence of the POD method, we have built enlarged snapshot sets, obtained by the action of the symmetry group of the problem on the original snapshot sets. The use of statistical symmetries of the flow in POD is discussed at length by Moin & Moser (1989) and Holmes, Lumley & Berkooz (1996).

In the uncoupled case, the problem satisfies four independent reflection symmetries S_x , S_y , S_z and S_d with respect to the planes $x = 0.5$, $y = 0.5$, $z = 0.5$ and $x = y$ (Puigjaner *et al.* 2008). In the coupled case, radiative transfer should break the S_z symmetry (radiative emission being proportional to T^4), but owing to the weak temperature gradients, nonlinear effects are negligible so that we can consider that the S_z symmetry is still satisfied. These four elementary symmetries generate a symmetry group of 16 elements. This allows us to multiply the number of snapshot by a factor of 16. In conclusion, for each simulation (coupled, uncoupled, $10^6 \leq Ra \leq 10^8$), we work on an enlarged snapshot set made of 16 000 samples (1000 original snapshots multiplied by 16 after applying all the symmetries).

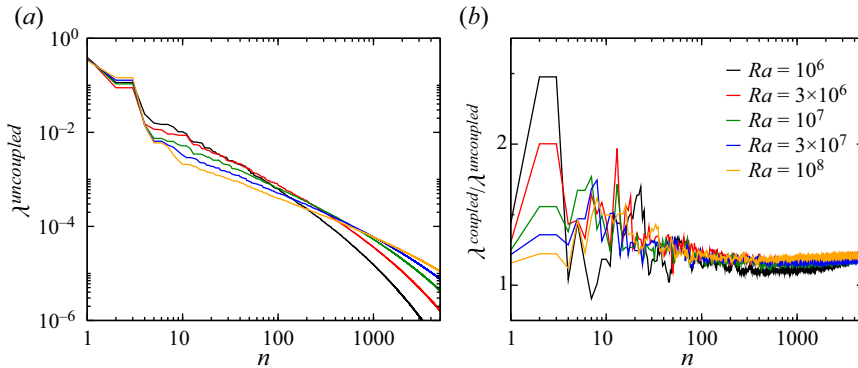


Figure 4. The POD eigenspectrum obtained from uncoupled simulations, normalised such that $\sum_n \lambda_n = 1$ (a) and POD eigenspectrum ratio between coupled and uncoupled results (b).

3.2. Energy spectra

The POD spectra obtained in the uncoupled case at different Rayleigh numbers are shown in figure 4(a). Each spectrum is normalised such that $\sum_n \lambda_n = 1$ but since the total POD energy is nearly constant with the Rayleigh number in the uncoupled case, it is relevant to compare the spectra between them. The mode ordering roughly corresponds to a ranking of the eigenfunctions in terms of a characteristic spatial scale, and we can therefore associate the low-order modes with the largest spatial scales and the high-order modes with the smallest spatial scales. Examination of figure 4 suggests that the POD spectra can be split into three parts: (i) the large scales for $n \lesssim 10$ which will correspond to the modes retain in the models in § 4; (ii) the intermediate scales for $10 \lesssim n \lesssim N$, with N such that the N first POD modes capture 95% of the total energy (N increases with the Rayleigh number, it goes from 250 at $Ra = 10^6$ to approximately 5000 at $Ra = 10^8$); (iii) the small scales for $n \gtrsim N$. At high Rayleigh number ($Ra = 3 \times 10^7$, $Ra = 10^8$), there is a different behaviour of large scales and intermediate scales, with a very fast decay of the low-order modes followed by a very slow decay in the rest of the spectrum owing to the turbulent nature of the flow. On the contrary, at low Rayleigh number ($Ra = 10^6$, $Ra = 3 \times 10^6$), the energy contained in the intermediate scales is proportionately more important and a fast decay of the energy of the small scales is observed. Interestingly, the spectrum decay is roughly log-linear in the intermediate range and this will be used in § 6 to model the variations of the POD spectrum with the Rayleigh number.

Figure 4(b) shows the ratio between the coupled POD spectrum and the uncoupled POD spectrum at each Rayleigh number. This ratio is always greater than one (except for one mode at $Ra = 10^6$) which confirms that the coupled POD spectrum captures the energy increase associated with radiation effects. However, this energy increase depends on the Rayleigh number and on the part of the spectrum. At low Rayleigh number, the energy increase is proportionately higher in the large-scale range, while at high Rayleigh number, the energy increase is proportionately higher in the intermediate scale range. In the small-scale range, the spectrum ratio is nearly constant and remains greater than one. As expected from the discussion in § 2.3, the ratio between coupled and uncoupled total POD energies decreases with the Rayleigh number as radiation effects weaken: it is equal to 1.59 at $Ra = 10^6$ and equal to 1.19 at $Ra = 10^8$.

A last parameter characterising the POD spectra is the factor γ , the values of which are reported in table 3. This factor γ (corresponding to the ratio between mechanical energy and thermal energy, see (3.3)) increases with the Rayleigh number and is always greater

Ra	10^6	3×10^6	10^7	3×10^7	10^8
Uncoupled	0.95	1.10	1.30	1.50	1.75
Coupled	1.17	1.24	1.42	1.62	1.85

Table 3. The γ factor for uncoupled and coupled cases at different Rayleigh numbers.

in the coupled case at a given Rayleigh number, which is consistent with the observations of [figure 1](#).

3.3. Spatial eigenfunctions

3.3.1. Uncoupled case, $Ra = 10^6$

[Figure 5](#) shows the first 12 POD eigenfunctions at $Ra = 10^6$ in the uncoupled case, which correspond to nine spatial structures (three of the modes are doubly degenerated). The figure displays the contribution of each structure to the mean convective heat flux in the vertical direction which can be written as $\sqrt{Ra} \sum_n \lambda_n \phi_n^\theta \phi_n^w$ owing to the POD decomposition. Five spatial structures have been already highlighted in previous works (Soucasse *et al.* 2019, 2020) and correspond to the first seven POD modes at $Ra = 10^7$. They are labelled M , $L_{x/y}$, D , $BL_{x/y}$ and C . We briefly mention their properties and physical meaning.

- (i) The M mode corresponds to the mean flow: it is made of two counter rotating torus and it is thermally stratified.
- (ii) The L_x and L_y modes form a pair of degenerate modes (only the L_x mode is shown in [figure 5](#), the L_y mode is its image by a rotation of $\pi/2$ around the vertical axis). They correspond to a single large-scale roll lying in either x planes or y planes. When combined, the L_x and L_y modes form a single large-scale diagonal roll.
- (iii) The D mode is an 8-roll mode that transports fluid from one corner to the other and strengthens the circulation along the diagonal.
- (iv) The BL_x and BL_y modes (pair of degenerate modes) are constituted of two longitudinal corotating structures around the x axis or the y axis. They connect the core of the cell with the horizontal boundary layers.
- (v) The C mode is a corner-roll mode which favours planar flow states and was found to promote reorientations between diagonal flow states.

In addition, four other spatial structures are noticeable in [figure 5](#). They are labelled D^* , C^* , $BL_{x/y}^*$ and M^* because they share common features with modes D , C , $BL_{x/y}$ and M .

- (i) The D^* mode is a 4-roll mode that shares some similarities with the D mode, as it transports fluid from one corner to the other. However, the rolls of the D^* mode extend from bottom to top, while the rolls of the D mode are confined in either the upper half or the lower half of the cell.
- (ii) The C^* mode is another corner-roll mode. Unlike the C -mode these corner rolls extend from top to bottom and are not confined in a half-cell.
- (iii) The BL_x^* and BL_y^* modes (pair of degenerate modes) are made of two longitudinal counter-rotating structures around the x or the y axis. A two-dimensional version of these POD modes has been highlighted by Podvin & Sergent (2017) in the square cell (symmetry-breaking mode labelled S).

Low-order models for radiation effects on RB convection

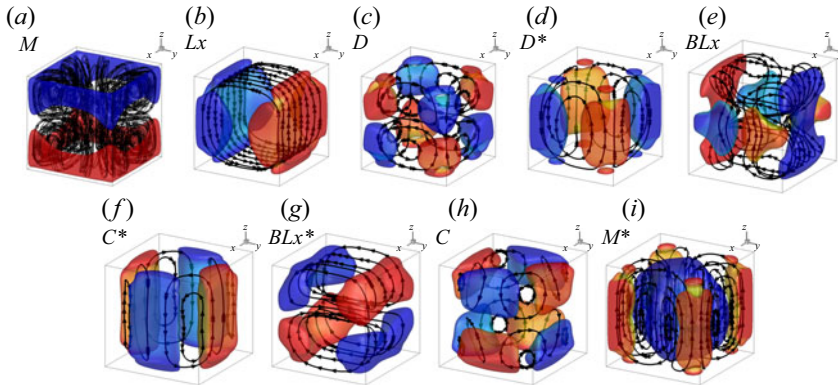


Figure 5. First 12 modes at $Ra = 10^6$ (uncoupled case). Streamlines and isosurfaces of the contribution to the mean convective heat flux $\phi^\theta \phi^w = 0.25$, coloured by mode temperature. For degenerate modes, only the x -oriented one is displayed. Colour map for mode temperature ranges from -0.5 (blue) to 0.5 (red).

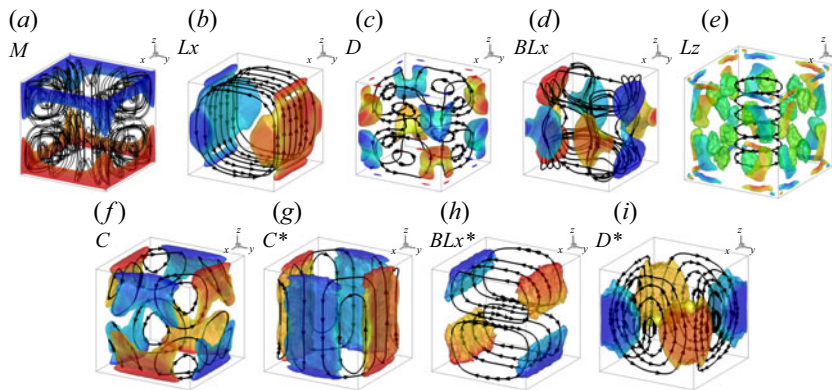


Figure 6. First 12 modes at $Ra = 10^8$ (uncoupled case). Streamlines and isosurfaces of the contribution to the mean convective heat flux $\phi^\theta \phi^w = 0.25$ (0.025 for the L_z mode), coloured by mode temperature. For degenerate modes, only the x -oriented one is displayed. Colour map for mode temperature ranges from -0.5 (blue) to 0.5 (red).

- (iv) The M^* mode is a single toroidal structure linking the top and bottom walls. The fluid flows up along the adiabatic vertical walls and flows down in the centre of the cell.

3.3.2. Uncoupled case, $Ra = 10^8$

Figure 6 shows the first 12 POD eigenfunctions at $Ra = 10^8$ in the uncoupled case. Despite the large difference in Rayleigh number, most of the modes observed at $Ra = 10^6$ are retrieved. One can identify again modes M , $L_{x/y}$, D , $BL_{x/y}$, C , as well as modes D^* , C^* and $BL_{x/y}^*$. However, the mode ordering is not exactly the same. In addition, streamlines and isosurfaces of convective heat flux in figure 6 are closer to the walls than those in figure 5, as boundary layers are thinner when the Rayleigh number increases. The M^* mode is no longer observed, but a new mode, the L_z mode, appears. This mode is constituted of a single roll lying in z plane. This is a pure mechanical mode ($\|\phi^u\| \simeq 1$) and one can note that the convective heat flux associated with the L_z mode is much weaker than that of the other modes.

3.3.3. Other coupled and uncoupled cases, similarities

For the other cases studied (other Rayleigh numbers, coupled with radiation), the first 12 POD modes belong to the set of the thirteen POD modes described above: M , $L_{x/y}$, D , $BL_{x/y}$, C , D^* , C^* , $BL_{x/y}^*$, M^* and L_z . The list of the modes, ordered according to their eigenvalue, is given in [table 4](#). A remarkable feature is that the eigenfunctions are globally preserved when radiation is taken into account, although the associated eigenvalues are higher than in the uncoupled case. In the range $10^7 \leq Ra \leq 10^8$, there are very few differences in the mode ordering, whatever the coupling conditions. It can be noted that the L_z mode becomes more important when the Rayleigh number increases and when radiation is considered. In the range $10^6 \leq Ra \leq 3 \times 10^6$, the mode ordering is less stable. Indeed, the eigenvalues of the modes are closer to each other, given the slower decay of the POD spectrum at low Rayleigh number. The ordering observed in the coupled case at $Ra = 10^6$ is the most different from the others: the D mode is no longer in fourth position, the $BL_{x/y}$ modes are also downshift far from the first modes and both M^* and L_z modes are present. This is not surprising as this case is the only one associated with quasi-stable planar flow states.

The question arising is: How close are two eigenfunctions of the same nature but belonging to different POD bases (for instance the D mode in the uncoupled case at $Ra = 10^6$ and the D mode in the coupled case at $Ra = 3 \times 10^7$)? To answer this, we have taken the POD basis of the uncoupled case at $Ra = 10^7$ as a reference and we have computed, for a given POD basis \mathcal{B} , the differences compared with this reference using the following error measure:

$$e^{\mathcal{B}} = \sqrt{\sum_{n=1}^{12} \frac{1}{12} \left(1 - \left| \int \phi_n^{\mathcal{B}}(\mathbf{r}) \cdot \phi_n^{ref}(\mathbf{r}) \, d\mathbf{r} \right| \right)}, \quad (3.4)$$

where ϕ_n^{ref} are the eigenfunctions of the reference POD basis and $\phi_n^{\mathcal{B}}$ are the eigenfunctions of the POD basis \mathcal{B} , reordered according to the mode ranking of the reference case. For the L_z mode, which is not contained in the reference basis, we have taken the L_z mode obtained at $Ra = 10^7$ in the coupled case as the reference. Values of indicator $e^{\mathcal{B}}$ are reported in [table 4](#). The differences compared with the reference basis are rather small and are approximately 1% or less, except for the coupled case at $Ra = 10^6$. This result will be key for the development of a POD model across the Rayleigh range (see § 6) and for predicting radiative transfer effects.

A last comment on the 13 identified modes can be made regarding their contribution to the global angular momentum and their symmetry properties, given in [table 5](#). The symmetry analysis sheds light on mode interactions in the low-order models and the angular momentum is used to monitor the flow reorientations. The modes contributing to the x and y components of the angular momentum are of course the LSC modes L_x and L_y but also, in a lesser extent the boundary layer modes BL_x and BL_y . Furthermore, the L_x and the BL_x modes have the same symmetry properties, as well as the L_y and the BL_y modes. It denotes strong interactions between these two pairs of modes, corresponding to the connection between the LSC and the boundary layers. Interestingly, all the degenerate modes break the S_d symmetry and each pair possesses opposite symmetry properties in S_x and S_y . In addition, one can note that D^* , C^* , $BL_{x/y}^*$ and M^* modes have the same symmetry properties in S_x , S_y and S_d as their companion mode D , C , $BL_{x/y}$ and M , but have opposite symmetry properties in S_z .

10^6		3×10^6		10^7		3×10^7		10^8	
Uncoupled	Coupled	Uncoupled	Coupled	Uncoupled	Coupled	Uncoupled	Coupled	Uncoupled	Coupled
M	M	M	M	M	M	M	M	M	M
$L_{x/y}$	$L_{x/y}$	$L_{x/y}$	$L_{x/y}$	$L_{x/y}$	$L_{x/y}$	$L_{x/y}$	$L_{x/y}$	$L_{x/y}$	$L_{x/y}$
D	C^*	D	D	D	D	D	D	D	D
D^*	M^*	D^*	C^*	$BL_{x/y}$	$BL_{x/y}$	$BL_{x/y}$	$BL_{x/y}$	$BL_{x/y}$	L_z
$BL_{x/y}$	C	C^*	$BL_{x/y}$	C	C	C	L_z	L_z	$BL_{x/y}$
C^*	D	$BL_{x/y}$	C	C^*	L_z	L_z	C	C	C
$BL_{x/y}^*$	L_z	C	M^*	D^*	C^*	C^*	C^*	C^*	C^*
C	$BL_{x/y}^*$	$BL_{x/y}^*$	D^*	$BL_{x/y}^*$	D^*	D^*	D^*	$BL_{x/y}^*$	$BL_{x/y}^*$
M^*	$BL_{x/y}$	M^*	$BL_{x/y}^*$	M^*	$BL_{x/y}^*$	$BL_{x/y}^*$	$BL_{x/y}^*$	D^*	D^*
1.14	5.60	0.516	0.974	N/A	0.406	0.526	0.735	1.23	1.37

Table 4. List of the first 12 POD modes for each case studied, ordered from top to bottom. The last line of the table gives the error measure e^B in percentage between the POD basis and the reference POD basis ($Ra = 10^7$, uncoupled) as defined in (3.4).

Mode name	L_x	L_y	L_z	Symmetries			
M	—	—	—	S_x	S_y	S_z	S_d
L_x	X	—	—	S_x	AS_y	AS_z	—
L_y	—	X	—	AS_x	S_y	AS_z	—
D	—	—	—	AS_x	AS_y	S_z	S_d
BL_x	X	—	—	S_x	AS_y	AS_z	—
BL_y	—	X	—	AS_x	S_y	AS_z	—
C	—	—	—	S_x	S_y	S_z	AS_d
D^*	—	—	—	AS_x	AS_y	AS_z	S_d
BL_x^*	—	—	—	S_x	AS_y	S_z	—
BL_y^*	—	—	—	AS_x	S_y	S_z	—
C^*	—	—	—	S_x	S_y	AS_z	AS_d
M^*	—	—	—	S_x	S_y	AS_z	S_d
L_z	—	—	X	AS_x	AS_y	S_z	AS_d

Table 5. Name, angular momentum and symmetry properties of the 13 identified modes. An X indicates a non-zero angular momentum. Here $S_{x/y/z/d}$ and $AS_{x/y/z/d}$ denote, respectively, a symmetry and an antisymmetry with respect to the planes $x = 0.5$, $y = 0.5$, $z = 0.5$ and $x = y$.

4. Uncoupled models

In this section we derive low-order models for the uncoupled case from uncoupled DNS data. We consider two different truncations: a 6-D truncation, with modes $L_{x/y}$, D , $BL_{x/y}$ and C , and a 11-D truncation, with in addition modes D^* , C^* , $BL_{x/y}^*$, M^* or L_z modes. The mode M , corresponding to the mean flow, is always taken as constant.

4.1. Construction

Proper orthogonal decomposition low-order models are derived from Galerkin projection of Navier–Stokes equations ((2.3)–(2.4)) onto a POD basis set. Using the decomposition (3.2), this yields a system of ordinary differential equations for the mode amplitudes $a_n(t)$ of the form

$$\frac{da_n(t)}{dt} = (L_{nm}^B + L_{nm}^D)a_m(t) + Q_{nmp}a_m(t)a_p(t) + T_n(t), \quad (4.1)$$

where L_{nm}^B and L_{nm}^D are linear coefficients associated with buoyancy and diffusion and Q_{nmp} are quadratic coefficients associated with advection. They are directly determined from spatial modes ϕ_n , see Appendix A. Here $T_n(t)$ is a closure term, which models the effect of the truncation and corresponds to an equivalent dissipation term. Following Podvin & Sergent (2015), the closure term is expressed as a combination of linear and cubic terms, and by the addition of noise such that

$$T_n(t) = L_{nm}^A \left(1 + \frac{1}{\langle k \rangle} \sum_{p \geq 2} |a_p(t)|^2 \right) a_m(t) + \sigma \epsilon_n(t), \quad (4.2)$$

where L_{nm}^A are adjustable linear parameters, $\langle k \rangle$ is the time average of the energy of the fluctuating modes in the truncation and $\epsilon_n(t)$ is a random noise perturbation of amplitude one.

The adjustable coefficients L_{nm}^A were determined for equilibria $a_n(t) = a_n^{eq}$ corresponding to diagonal states from the DNS ($da_n^{eq}/dt = 0$). We retain the following

equilibrium: $a_M^{eq} = \sqrt{\lambda_M}$; $a_{L_{x/y}}^{eq} = \sqrt{\lambda_{L_{x/y}}}$; $a_D^{eq} = \sqrt{\lambda_D}$; $a_{BL_{x/y}}^{eq} = -\eta_{BL}\sqrt{\lambda_{BL_{x/y}}}$ and $a_n^{eq} = 0$ for the other modes. Note that boundary layer modes $BL_{x/y}$ are negatively correlated with LSC modes $L_{x/y}$ and their equilibrium value in absolute value $|a_{BL_{x/y}}^{eq}|$ is smaller than the standard deviation of their fluctuations ($\eta_{BL} < 1$). The coefficient η_{BL} is approximately 0.15–0.2 except at $Ra = 10^8$ where it is much weaker ($\eta_{BL} = 0.05$). A large value of η represents a strong connection between the boundary layers and the LSC in the diagonal state. The coefficients L_{nm}^A can only be determined unambiguously for modes M , $L_{x,y}$, D and $BL_{x,y}$, which are non-zero at equilibrium. For modes which are zero at equilibrium, the sum of linear contributions was adjusted to balance quadratic interactions with the mean mode, in order to avoid excessive energy. We checked that the model behaviour did not change when small changes were made in the adjustable parameters.

The noise level was estimated as follows:

$$\sigma = C \frac{\sum_8^{2000} \lambda_n}{\sqrt{\sum_2^7 \lambda_n}}, \tag{4.3}$$

where $C = 0.016$ is a constant, determined at $Ra = 10^7$ from a scaling analysis (Soucassee *et al.* 2019). The ratio in (4.3) gives a rough estimate of the energy transferred from the low-order truncation to the next higher-order scales. This ratio reaches a maximum at $Ra = 3 \times 10^6$ and is lowest for the highest Rayleigh numbers. The noise level is indicated in Appendix A.

4.2. Time integration

The dynamics of modes $L_{x/y}, D$, C and $BL_{x/y}$ have already been discussed in previous work for the case $Ra = 10^7$ (Soucassee *et al.* 2019). We checked that the general features of the phase portraits held over the range of Rayleigh numbers considered. In particular, the following points were established.

- (i) Quasi-steady states constituting the LSC are characterised by roll $L_{x/y}$ and boundary layer modes $BL_{x/y}$ connecting the boundary layer and the core region.
- (ii) The mode D indicates along which diagonal the LSC takes place and tends to stabilise the LSC.
- (iii) The corner mode C is essential to reproduce reorientations in the model. The frequency of reorientations also depends on the coupling between the boundary layer modes and the roll modes, as well as on the noise level. A higher intensity of the boundary layer mode makes the LSC less likely to become unstable.

Figure 7 shows histograms of modes L_x and L_y at different Rayleigh numbers obtained with the 11-D model and with the DNS. They have been computed from time series of mode amplitudes a_{L_x} and a_{L_y} and represent the probability density function of the flow in the phase space L_x – L_y . It can be seen that the model captures the change in dynamics with the Rayleigh number: the planar states are more frequently visited at low Rayleigh number and the stability of the diagonal states increases at high Rayleigh number.

This is further confirmed by the values of reorientation frequencies. Frequencies of zero crossings for modes L_x , L_y and D , for the uncoupled DNS and model are reported in table 6. Frequency f_D corresponds to the reorientation frequency f_r defined in § 2.3, as the D mode changes sign at each reorientation. Values for the model reported in the table were obtained for an integration time of 40 000 time units. Uncertainties on model

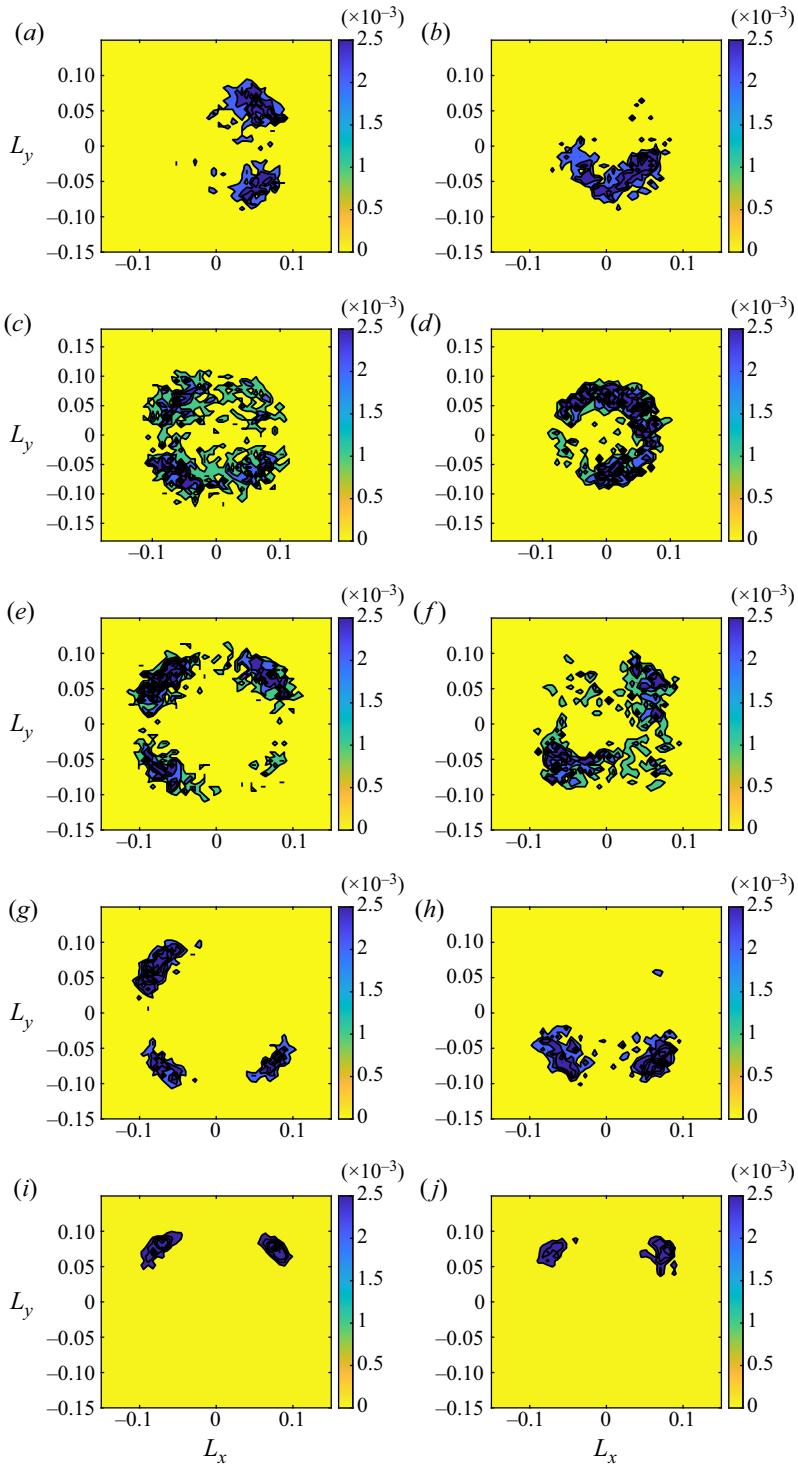


Figure 7. Histograms of modes L_x and L_y : DNS (*a,c,e,g,i*) and model (*b,d,f,h,j*). Uncoupled case with integration time for the model equal to Δt (DNS). Rayleigh numbers are: (*a,b*) $Ra = 10^6$; (*c,d*) $Ra = 3 \times 10^6$; (*e,f*) $Ra = 10^7$; (*g,h*) $Ra = 3 \times 10^7$; (*i,j*) $Ra = 10^8$.

Ra	Uncoupled model					
	$f_{L_x} \times 10^3$		$f_{L_y} \times 10^3$		$f_D \times 10^3$	
	DNS	model	DNS	model	DNS	model
10^6	0.8	1.1	0.9	1.1	1.3	1.7
3×10^6	1.4	1.4	1.0	1.1	2.2	1.7
10^7	0.8	0.8	0.7	1.0	1.4	1.3
3×10^7	N/A	0.4	N/A	0.3	0.4	0.8
10^8	N/A	N/A	N/A	0.05	N/A	0.14

Table 6. Average frequencies $f_n = 1/\tau_n$ in the uncoupled DNS and in the uncoupled model where τ_n is the average time between zeros of a_n (restricted to times larger than $5\tau_c$). The value N/A is indicated when it was not possible to obtain a value (less than two switches observed at higher Rayleigh numbers). Integration time for the model is 40 000 time units.

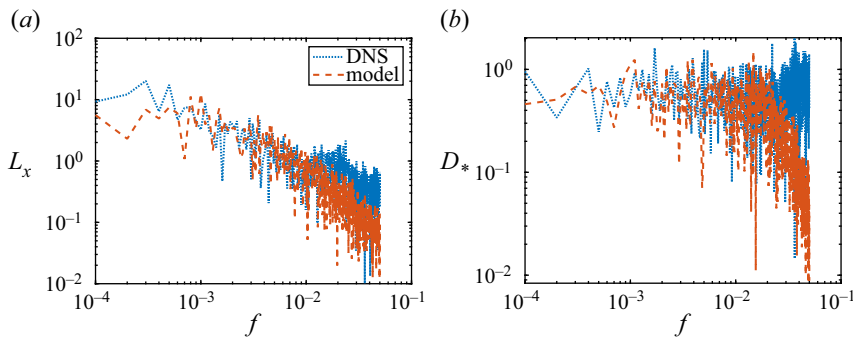


Figure 8. The DNS and model spectra at $Ra = 3 \times 10^6$ for mode L_x (a) and mode D^* (b).

frequencies are approximately four to eight times smaller than uncertainties on DNS frequencies, according to the respective integration times. It can be noted in table 6 that the model captures the decrease of reorientation frequencies with the Rayleigh number and fairly reproduces the frequencies observed in the DNS. Discrepancies between DNS and model results are of the order of the uncertainty on DNS frequencies (see table 2). At the higher Rayleigh numbers, we found that it is not always possible to determine reorientation frequencies in the DNS as the available simulation time is relatively small compared with the characteristic time between reorientations. However, it was possible to obtain values for the model since the integration time could be easily extended.

Time spectra of roll mode L_x and higher-order mode D^* are represented in figure 8 and compared with the DNS at $Ra = 3 \times 10^6$. A good agreement is observed for frequencies up to 10^{-2} . However, the model is not able to predict the local increase of the circulation frequency $f_c \sim 2 \times 10^{-2}$ and the energetic content at higher frequencies is underpredicted, which is not surprising given the small size of the truncation.

4.3. Effects of the additional modes

We study in this section the effects of the additional modes included in the 11-D truncation: modes D^* , C^* , $BL_{x/y}^*$, M^* (for $Ra \leq 10^7$) and L_z (for $Ra \geq 3 \times 10^7$). Modes L_z and M^* , respectively, correspond to a toroidal and poloidal circulation in the cube.

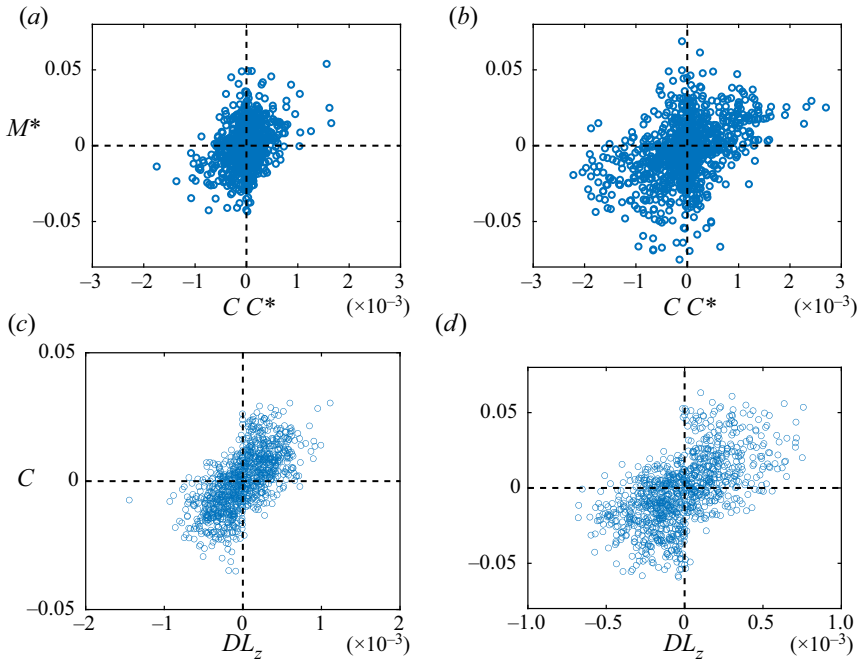


Figure 9. (a,b) Phase portrait of M^* and CC^* in the DNS (a) and in the model (b) at $Ra = 10^7$; (c,d) the phase portrait of C and DL_z in the DNS (c) and in the model (d) at $Ra = 10^8$.

These differences correspond to different interactions with other modes: the evolution of mode $L_{x,y}$ is determined by the interaction of M^* with mode $BL_{x,y}^*$, as well as mode L_z with mode $BL_{x,y}$. Moreover, the dynamics of M^* depends on interactions between modes L and BL , modes BL and BL^* with the same orientation (x or y), as well as interactions of mode C and C^* , and D and D^* . In contrast, the evolution of L_z depends on cross-interactions of modes C and D , as well as C^* and D^* , and modes L and BL corresponding to different directions (x and y). Phase portraits in figure 9 show that the correlations observed in the DNS are reproduced by the model. More quantitatively, the correlation coefficient between modes C and product DL_z at $Ra = 10^8$ is equal to 0.66 in both the model and the DNS. At $Ra = 10^7$, the correlation coefficient between modes M^* and product CC^* is equal to 0.5 in the model and 0.3 in the DNS.

To get further insights on the effects of the additional modes, we have compared the dynamics of the model using either the 11-D truncation or the 6-D truncation. Generally speaking, the results obtained with the 6-D truncation are very similar to those obtained with the 11-D truncation, which means the additional modes do not alter the general dynamics of the reorientations. Reorientation frequencies given in table 6 are retrieved with the 6-D model within the same accuracy. This small influence of the additional modes is further confirmed by a linear stability analysis performed around diagonal equilibria for both truncations at each Rayleigh number. The resulting eigenvalue spectra are given in figure 10. First, it can be noted that the shape of the spectrum is globally preserved with the Rayleigh number. Comparison of the 6-D and the 11-D truncations shows that the 6-D reproduces the essential features of the 11-D truncation, that is: (i) a pair of very stable eigenvalues associated with an eigenvector with a strong component along the D mode; (ii) two real eigenvalues associated with eigenvectors coupling $L_{x/y}$ and $BL_{x/y}$ modes;

Low-order models for radiation effects on RB convection

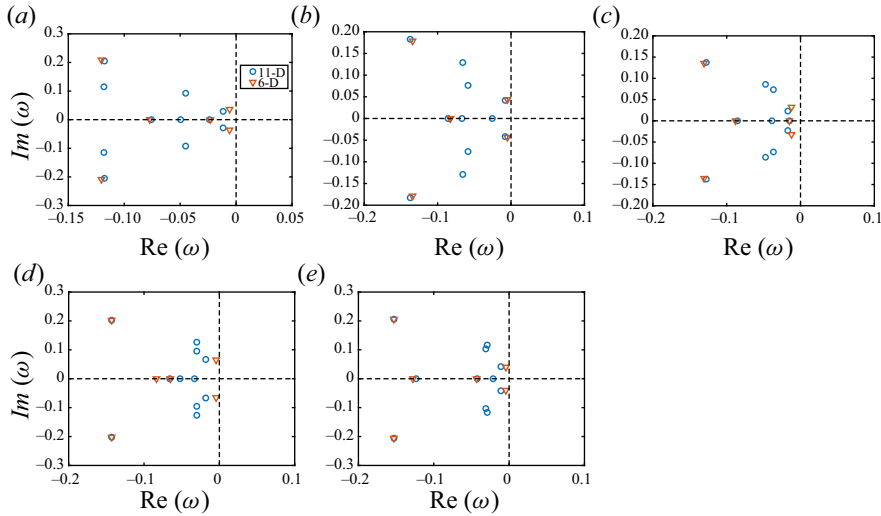


Figure 10. Linear stability analysis spectrum around the (L_x, L_y) equilibria. Comparison between the 6-D and 11-D truncations of the uncoupled model. Rayleigh numbers are (a) $Ra = 10^6$; (b) $Ra = 3 \times 10^6$; (c) $Ra = 10^7$; (d) $Ra = 3 \times 10^7$; (e) $Ra = 10^8$.

(iii) a pair of eigenvalues close to the stability limit associated with an eigenvector with a strong C component. This last point confirms the key role of the corner flows associated with the C mode in the reorientation process, even at low Rayleigh number where the energy of this mode is proportionately weaker. In addition, the 11-D spectrum contains one real eigenvalue, associated with either L_z or M^* , and two additional pairs of complex eigenvalues associated with modes C^* and $BL_{x/y}^*$, and D^* and $BL_{x/y}^*$. These two pairs of eigenvalues are close to each other, except at $Ra = 10^6$, where the real part of the eigenvalues associated with D^* and modes $BL_{x/y}^*$ is much more stable than at all other Rayleigh numbers.

5. Predicted coupled models

We derive in this section low-order models that include radiation effects. These models are referred to as predicted coupled models because they only rely on uncoupled DNS data and correspond to an *a priori* attempt to model radiation effects.

5.1. Construction

In the framework of the Boussinesq approximation (weak temperature differences), the temperature dependence of the radiation field can be assumed to be linear. We are therefore able to define a modal-radiative power $\mathcal{P}_n^{rad}(\mathbf{r})$, corresponding to the radiative response to a temperature eigenfunction $\phi_n^\theta(\mathbf{r})$ and such that $\mathcal{P}^{rad}(\mathbf{r}, t) = \sum_n a_n(t) \mathcal{P}_n^{rad}(\mathbf{r})$. Using this decomposition in the energy balance and applying Galerkin projection, a linear radiation term is obtained and the coupled POD model takes the general form

$$\frac{da_n(t)}{dt} = (L_{nm}^B + L_{nm}^D + L_{nm}^R) a_m(t) + Q_{nmp} a_m(t) a_p(t) + T_n(t), \quad (5.1)$$

where L_{nm}^R are linear radiation coefficients. Definition and computation details for coefficients L_{nm}^R and for the modal radiative power $\mathcal{P}_n^{rad}(\mathbf{r})$ are given in [Appendix B](#) and

can be also found in Soucasse *et al.* (2020). We will assume that the form of the closure law (see (4.2)) remains valid in the presence of radiation.

Our goal is to build an *a priori* model of radiative transfer effects based on uncoupled DNS data and uncoupled POD eigenfunctions. Therefore, model coefficients are determined as follows:

- (i) Coefficients L_{nm}^B , L_{nm}^D and Q_{nmp} are taken from the uncoupled model.
- (ii) Coefficients L_{nm}^R are added and computed from uncoupled temperature eigenfunctions ϕ_n^θ and uncoupled factor γ .
- (iii) Adjustable coefficients L_{nm}^A are taken from the uncoupled model. This means we assume that the energy transfer from the large scales to the small scales is unchanged.

However, equilibrium values of mode amplitude $a_n^{eq,rad}$ are required in the coupled model to estimate the contribution of the mean mode M , to estimate the fluctuating energy $\langle k \rangle$ in (4.2) and to estimate the noise level. They are not known *a priori* and need to be predicted. To do so, we use equilibrium relations ($da_n^{eq,rad}/dt = 0$) for diagonal states, with the additional radiation terms, the adjustable coefficients being known. Predicted equilibria $\tilde{a}_n^{eq,rad}$ for modes M , $L_{x/y}$, D and $BL_{x/y}$ are given in table 7 ($a_n^{eq,rad} = 0$ for the other modes) and compared with actual coupled equilibria $a_n^{eq,rad}$ and uncoupled equilibria a_n^{eq} extracted from the DNS. We can see that the effect of radiative coupling is to increase the energy of the equilibria, by lesser amounts as the Rayleigh number increases. Finally, the noise level in the coupled model σ^{rad} is determined from the energy increase of the large-scale modes compared with the uncoupled case

$$\frac{\sigma^{rad}}{\sigma} = \sqrt{\frac{\sum_n (\tilde{a}_n^{eq,rad})^2}{\sum_n (a_n^{eq})^2}}. \tag{5.2}$$

Noise level values are reported in Appendix A. As expected, the noise level with radiation σ^{rad} is always greater than the noise level without radiation due to the energy increase.

5.2. Mode energies

The predicted coupled model was then integrated in time, using an 11-D truncation, leading to predicted amplitudes a_i^{rad} . The predicted energy (or predicted eigenvalue) of the modes with radiative coupling $\tilde{\lambda}^{rad}$ was then determined using:

- (a) the ratio η_n determined above for the non-zero equilibrium values $\eta_n = (\tilde{a}_n^{eq,rad}/a_n^{eq})^2$ (with n corresponding to modes M , $L_{x,y}$, D , $BL_{x,y}$);
- (b) the ratio $\tilde{\eta}_n$ predicted from the model $\tilde{\eta}_n = \langle (a_n^{rad})^2 \rangle / \langle a_n^2 \rangle$ for modes which are zero at equilibria (with n corresponding to modes D^* , C , C^* , $BL_{x,y}^*$, L_z or M_z).

Figure 11 compares for each mode and each Rayleigh number the predicted energy $\tilde{\lambda}_n^{rad}$ with the eigenvalues λ_n and λ_n^{rad} found in the uncoupled and coupled DNS. In addition, the values of the total energy contained in the first 12 modes are reported in table 8. Except for the lowest Rayleigh number, corresponding to a large radiative increase which is overpredicted by the model, the total energy increase is correctly predicted by the model (within approximately 10 % maximum). Overall, the model tends to overpredict the amplitude of the $BL_{x/y}$ modes (which are associated with the largest relative increase) and

Ra		M	$L_{x/y}$	D	$BL_{x/y}$
10^6	a_n^{eq}	0.131	0.071	0.033	-0.0033
	$a_n^{eq,rad}$	0.157 (1.2)	0.111 (1.5)	0.024 (0.7)	-0.0027 (0.8)
	$\tilde{a}_n^{eq,rad}$	0.262 (2.0)	0.089 (1.3)	0.052 (1.6)	-0.0069 (2.1)
3×10^6	a_n^{eq}	0.130	0.062	0.025	-0.0026
	$a_n^{eq,rad}$	0.149 (1.15)	0.087 (1.4)	0.030 (1.2)	-0.0033 (1.3)
	$\tilde{a}_n^{eq,rad}$	0.163 (1.25)	0.067 (1.1)	0.030 (1.2)	-0.0042 (1.6)
3×10^7	a_n^{eq}	0.122	0.073	0.024	-0.0020
	$a_n^{eq,rad}$	0.134 (1.1)	0.085 (1.2)	0.027 (1.1)	-0.0026 (1.3)
	$\tilde{a}_n^{eq,rad}$	0.130 (1.1)	0.075 (1.0)	0.026 (1.1)	-0.0022 (1.1)
10^8	a_n^{eq}	0.116	0.076	0.024	-0.0008
	$a_n^{eq,rad}$	0.125 (1.1)	0.084 (1.1)	0.025 (1.0)	-0.0009 (1.1)
	$\tilde{a}_n^{eq,rad}$	0.131 (1.1)	0.08 (1.05)	0.026 (1.1)	-0.0011 (1.2)

Table 7. Non-zero equilibrium values in the uncoupled (a_n^{eq}) and coupled ($a_n^{eq,rad}$) cases (extracted from the DNS) and predicted equilibrium values ($\tilde{}_n^{eq,rad}$) with the predicted coupled model. Relative ratios compared with the uncoupled case are indicated in parentheses.

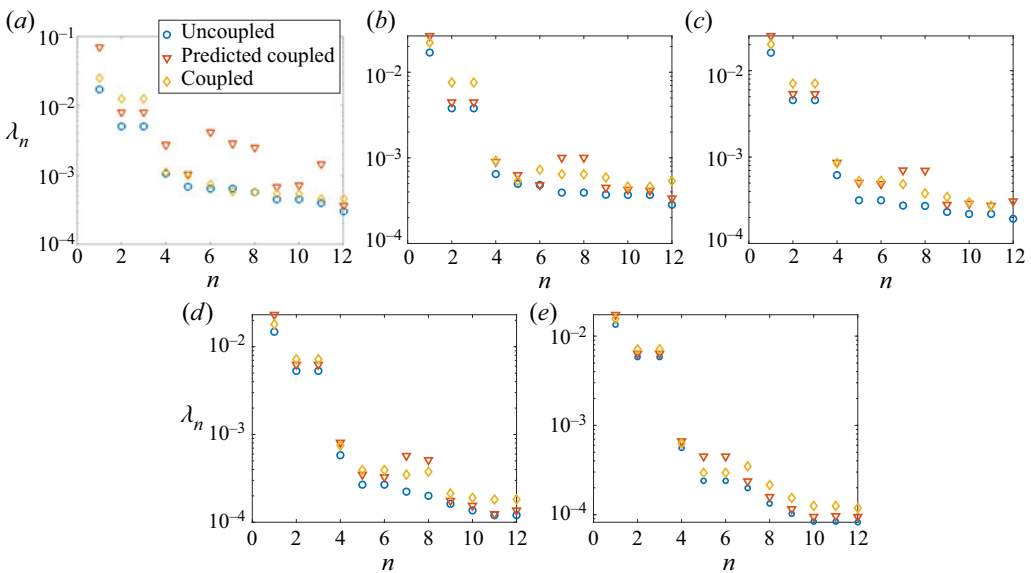


Figure 11. Predicted energies compared with POD eigenvalues in the uncoupled and coupled DNS. Energies are ranked according to the mode ordering in the uncoupled simulation. Rayleigh numbers are (a) $Ra = 10^6$; (b) $Ra = 3 \times 10^6$; (c) $Ra = 10^7$; (d) $Ra = 3 \times 10^7$; (e) $Ra = 10^8$.

underpredict that of the $L_{x/y}$ modes. However, the agreement is generally good, although the ordering of the modes observed in the coupled DNS is not always captured.

Figure 12 shows histograms of modes L_x and L_y at different Rayleigh numbers obtained with the coupled predicted model and the coupled DNS. At $Ra = 10^6$, the radiative coupling makes diagonal states unstable, and the LSC in the simulation tends to become parallel to the cavity sides. This change in dynamics is qualitatively predicted by the model: it can be seen in the histograms of figure 12 that the system spends considerable

Ra	10^6	3×10^6	10^7	3×10^7	10^8
$\sum_{n=1}^{12} \lambda_n$	0.0320	0.0281	0.0277	0.0275	0.0267
$\sum_{n=1}^{12} \lambda_n^{rad}$	0.0548 (1.71)	0.0425 (1.51)	0.0401 (1.44)	0.0353 (1.28)	0.0323 (1.21)
$\sum_{n=1}^{12} \tilde{\lambda}_n^{rad}$	0.0986 (3.08)	0.0405 (1.44)	0.0380 (1.37)	0.0388 (1.41)	0.0320 (1.20)

Table 8. Predicted energy (\sim) of the first 12 modes compared with eigenvalues in the uncoupled simulation λ_n and in the coupled simulation λ_n^{rad} . Relative ratios compared with the uncoupled case are indicated in parentheses.

time near the roll states ($L_x = 0$ or $L_y = 0$). This will be further confirmed by the linear stability analysis in § 5.4. At $Ra = 3 \times 10^6$, the coupled system seems to spend more time near the roll states although the diagonal states are still dominant. This is also correctly captured by the predicted model. Changes due to radiative coupling are less important at $Ra \geq 10^7$ in both the model and the DNS. At $Ra \geq 3 \times 10^7$, very few reorientations are observed and the amplitude of the oscillations about the equilibrium states decrease.

5.3. Reorientation frequencies

Table 9 compares frequencies of zero crossings for modes L_x , L_y and D , for the coupled DNS and the predicted coupled model. Generally speaking, a good agreement is observed between the predicted model and the coupled DNS (discrepancies of 10%–30%, of the order of the uncertainty on DNS frequencies), except at $Ra = 10^8$ where the reorientation frequency is underestimated. We note that results are not given for the coupled case at $Ra = 10^6$ since the diagonal states are no longer observed. We note that at $Ra = 3 \times 10^6$ large and fast oscillations in the D mode do not make it possible to determine a frequency in both the coupled simulation and the model. As in § 4.2, values for the model reported in the table were obtained for an integration time of 40 000 time units.

5.4. Model stability at $Ra = 10^6$

A remarkable feature of the predicted coupled model is its ability to predict the loss of stability of the diagonal rolls for the benefit of the planar rolls at $Ra = 10^6$. In fact, linear stability analysis of the diagonal equilibria for both 6-D and 11-D truncations (see figure 13) shows that the least stable pair of eigenvalues associated with mode C becomes markedly unstable with radiative coupling. Integration of the models without noise shows that in the presence of radiation the now unstable fixed point destabilises towards another fixed point in the $L_x = 0$ or $L_y = 0$ space (also in figure 13) corresponding to roll modes. We emphasise that both 6-D and 11-D truncations provide very similar results, indicating that the essential dynamics are captured by the 6-D truncation.

At other Rayleigh numbers, we found that for both 6-D and 11-D truncations the pair of eigenvectors associated with the corner mode C became less stable when radiation was taken into account, but their eigenvalue remained negative.

6. Generalised models over the Rayleigh number range

In this section, we develop a generalised model, for both uncoupled and coupled cases, that infers the dynamics over the Rayleigh number range from uncoupled DNS data at

Low-order models for radiation effects on RB convection

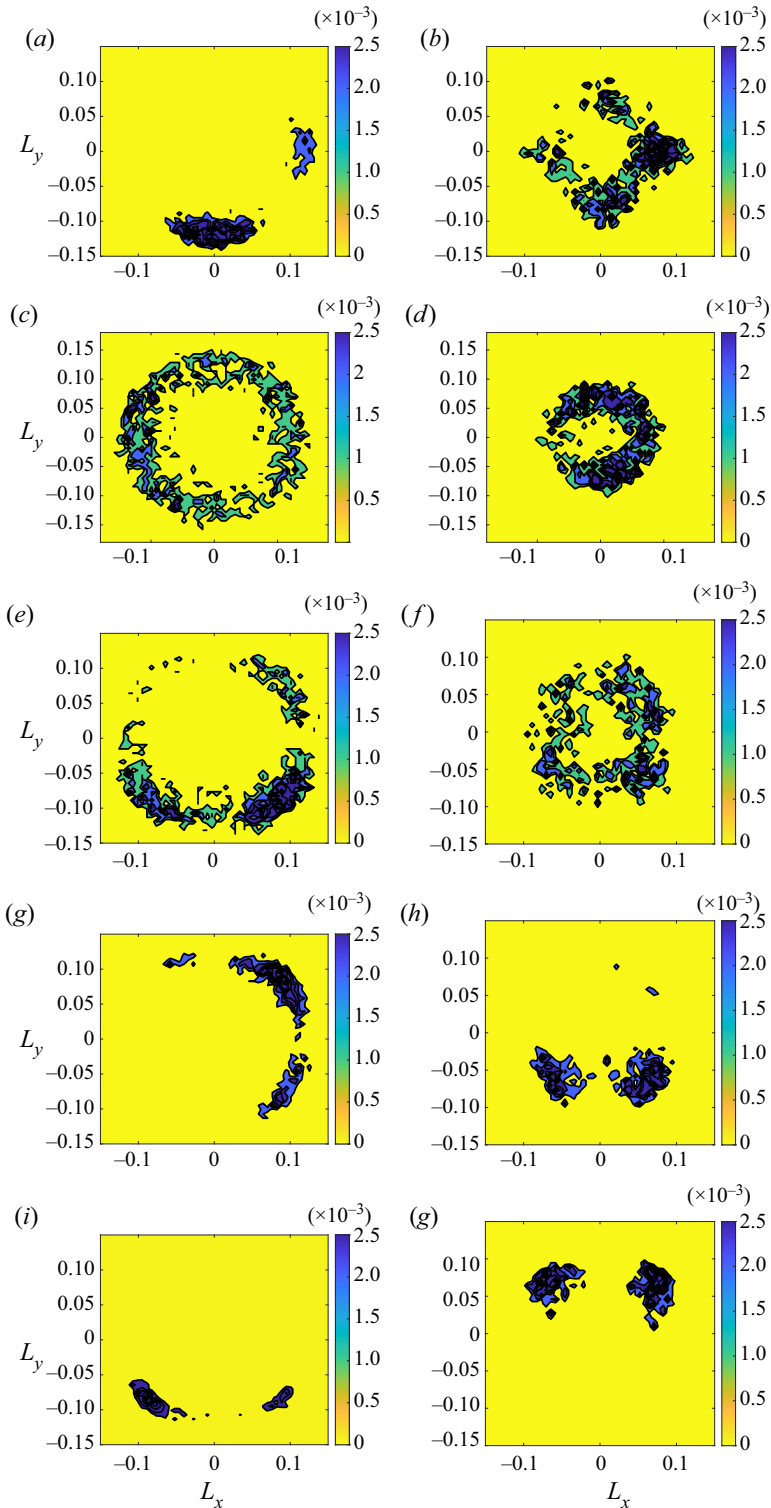


Figure 12. Histograms of modes L_x and L_y : DNS (a,c,e,g,i) and model (b,d,f,h,j). Coupled case with integration time for the model equal to Δt (DNS). Rayleigh numbers are (a,b) $Ra = 10^6$; (c,d) $Ra = 3 \times 10^6$; (e,f) $Ra = 10^7$; (g,h) $Ra = 3 \times 10^7$; (i,j) $Ra = 10^8$.

Ra	Coupled predicted model					
	$f_{L_x} \times 10^3$		$f_{L_y} \times 10^3$		$f_D \times 10^3$	
	DNS	model	DNS	model	DNS	model
3×10^6	1.6	1.5	1.2	1.4	N/A	N/A
10^7	0.9	1.2	0.7	1.0	1.7	1.7
3×10^7	0.4	0.5	0.4	0.5	1.3	0.9
10^8	1.1	N/A	N/A	0.1	1.1	0.2

Table 9. Average frequencies $f_n = 1/\tau_n$ in the coupled DNS and in the coupled model where τ_n is the average time between zeros of a_n (restricted to times larger than $5\tau_c$). The value N/A is indicated when it was not possible to obtain a value (less than two switches observed at higher Rayleigh numbers, many rapid switches at $Ra = 3 \times 10^6$). Integration time for the model is 40 000 time units.

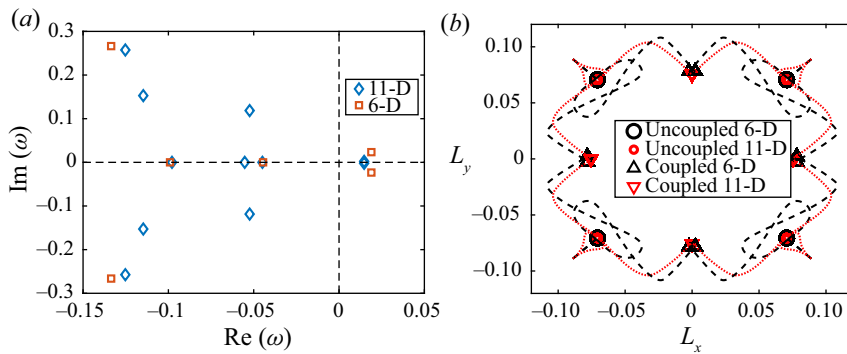


Figure 13. (a) Linear stability analysis spectrum around the (L_x, L_y) diagonal equilibria for the predicted coupled model at $Ra = 10^6$. (b) Trajectory in the (L_x, L_y) space of the coupled predicted model without noise from unstable diagonal equilibria: 6-D truncation (black dashed lines) and 11-D truncation (red dotted lines). Symbols indicate stable fixed point for both coupled and uncoupled models.

$Ra = 10^7$ and energy scaling laws. We restrict the models to a 6-D truncation with modes $L_{x/y}, D, BL_{x/y}$ and C .

6.1. Uncoupled case

The basic assumption in building the generalised model is that the variations of the eigenfunctions can be neglected over the Rayleigh number range. The key ingredient is thus to estimate correctly the distribution of the POD spectrum in order to determine the equilibria, the adjustable coefficients and the noise level. The form of the uncoupled generalised model is the same as that of the uncoupled model ((4.1) together with closure law (4.2)). Model parameters are determined as follows.

- (i) Linear and quadratic coefficients L_{nm}^B, L_{nm}^D and Q_{nmp} are directly determined from a set of POD eigenfunctions $\phi_n = \{\phi_n^u, \gamma \phi_n^\theta\}$. Here, ϕ_n^u and ϕ_n^θ are assumed to be constant with the Rayleigh number and taken at $Ra = 10^7$. The coefficient γ^2 is assumed to vary with the Rayleigh number according to the following law:

$$\gamma^2 \sim 0.032Ra^{1/4}, \tag{6.1}$$

which is consistent with the scaling of the turbulent fluctuations in the bulk $\theta^* \sim Ra^{-0.14}$ (Castaing *et al.* 1989).

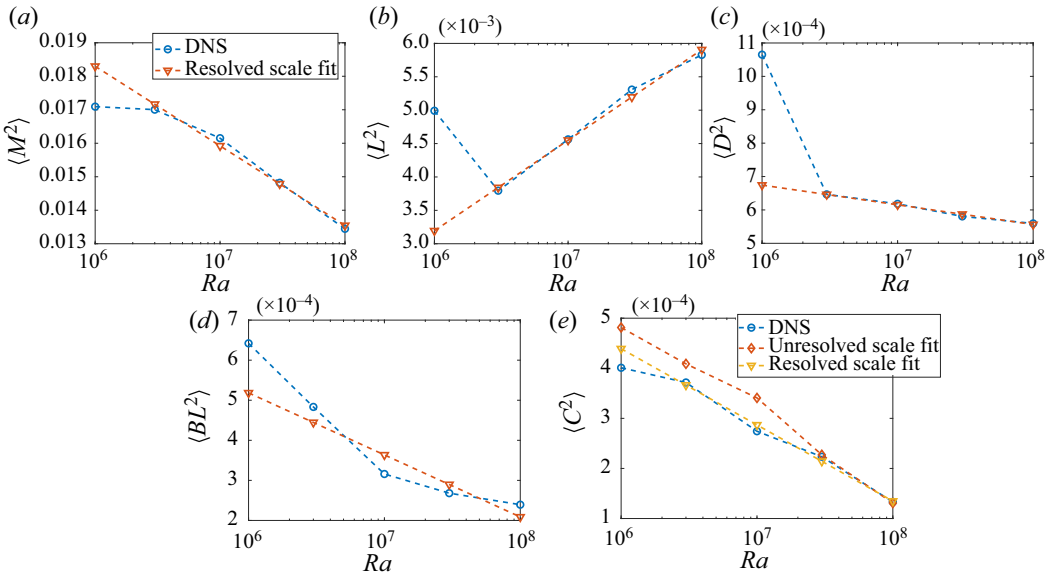


Figure 14. Evolution of the energy λ_n of the large-scale modes given by the DNS and the large-scale fit (6.2).

- (ii) The adjustable coefficients L_{nm}^A are determined from equilibrium relations for a diagonal state. Equilibrium values a_n^{eq} strongly depend on the Rayleigh number and are estimated using the following ansatz for the energy λ_n of the large-scale modes $n \in \{M, L_{x/y}, D, BL_{x,y}, C\}$:

$$\lambda_n = h_n \log(Ra) + g_n, \tag{6.2}$$

which is a good approximation at all Rayleigh numbers except the lowest one ($Ra = 10^6$), as it can be seen in figure 14. The lowest Rayleigh number was therefore not taken into account when fitting the coefficients h_n and g_n . Note that the ratio between the equilibrium value of modes $BL_{x/y}$ and their amplitude was taken to be constant and equal to $\eta_{BL} = 0.2$.

- (iii) As in § 4, the noise level is determined using (4.3), from the energy of the large scales and the energy of the intermediate scales. We have highlighted in § 3.2 that the spectrum decay of the intermediate scales is log-linear and we adopt the following modelling for their energy:

$$\lambda_n = C(Ra)n^{\alpha(Ra)} \quad \text{with} \quad \begin{cases} \log(C(Ra)) = 1.9 - 0.5 \log(Ra), \\ \alpha(Ra) = -2.0 + 0.07 \log(Ra). \end{cases} \tag{6.3}$$

The fit was determined from the variations of the spectrum λ_n with $8 \leq n \leq N/2$, with N such that the N first POD modes capture 95 % of the total energy. We have checked that the asymptotic decay was correctly captured. It can also be noted in figure 14 that the intermediate-scale fit provides a correct estimation of the energy of mode C , with a discrepancy between the large-scale and the intermediate-scale fit of 25 % maximum at the lowest Rayleigh number. Noise levels are reported in Appendix A.

The uncoupled generalised model was integrated in time for the different Rayleigh numbers. The measured reorientation frequencies are given in table 10. Overall, the

<i>Ra</i>	uncoupled generalised model					
	$f_{L_x} \times 10^3$		$f_{L_y} \times 10^3$		$f_D \times 10^3$	
	DNS	model	DNS	model	DNS	model
10^6	0.8	1.7	0.9	1.6	1.3	N/A
3×10^6	1.4	1.4	1.0	1.2	2.2	2.0
10^7	0.8	0.6	0.7	0.6	1.4	1.1
3×10^7	N/A	0.2	N/A	0.2	0.4	0.4
10^8	N/A	N/A	N/A	N/A	N/A	N/A

Table 10. Reorientation frequencies obtained with the uncoupled generalised model. Integration time for the model is 40 000 time units.

<i>Ra</i>	coupled generalised model					
	$f_{L_x} \times 10^3$		$f_{L_y} \times 10^3$		$f_D \times 10^3$	
	DNS	model	DNS	model	DNS	model
3×10^6	1.6	1.6	1.2	1.4	N/A	N/A
10^7	0.9	1.1	0.7	0.9	1.7	1.5
3×10^7	0.4	0.6	0.4	0.5	1.3	1.0
10^8	1.1	0.9	N/A	1.0	1.1	1.4

Table 11. Reorientation frequencies obtained with the coupled generalised model. Integration time for the model is 40 000 time units.

model correctly captures the amplitude of the modes and the associated time scales, except at $Ra = 10^6$. At this Rayleigh number, the energy of the large-scale modes is underestimated by the large-scale fit, which leads to an overestimation of the noise level and an overestimation of the reorientation frequency. At $Ra = 10^8$, no reorientation event has been detected by the model despite a large integration time.

6.2. Coupled case

Following the procedure described in § 5.1, radiation effects are incorporated in the generalised model. Model parameters for the coupled generalised model are thus determined as follows.

- (i) Coefficients L_{nm}^B , L_{nm}^D and Q_{nmp} are taken from the uncoupled generalised model.
- (ii) Coefficients L_{nm}^R are added and computed from uncoupled temperature eigenfunctions ϕ_n^θ at $Ra = 10^7$ and γ factor modelled by (6.1).
- (iii) Adjustable coefficients L_{nm}^A are taken from the uncoupled generalised model. This allows us to estimate equilibrium values $\tilde{a}_n^{eq,rad}$ and energies $\tilde{\lambda}_n^{rad}$ for the modes in the truncation (except mode C which is zero at equilibrium).
- (iv) The noise level is determined using (5.2).

Differences between all the models (uncoupled model, predicted coupled model, uncoupled generalised model and coupled generalised model) are highlighted in [Appendix A](#).

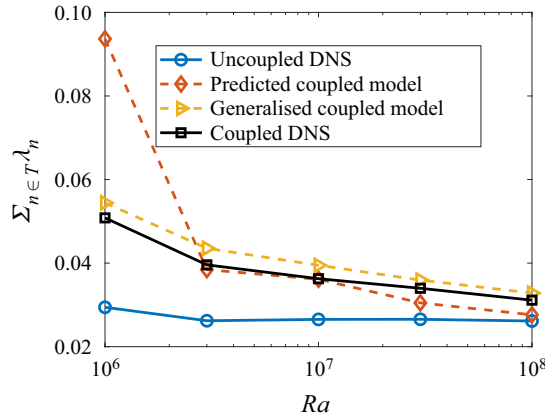


Figure 15. Total energy of the large-scale modes $\sum_{n=1}^7$ as a function of the Rayleigh number – comparison of the DNS, the coupled predicted model and the coupled generalised model.

The total energy of the large-scale modes $\sum_{n=1}^7 \tilde{\lambda}_n^{rad}$ predicted by the coupled generalised model is represented in figure 15 and compared with values given by the coupled DNS and the coupled predicted model. In addition, the energy increase for each large-scale mode $M, L_{x,y}, D, BL_{x,y}$ is given in figure 16. In terms of total large-scale energy, a very good agreement is observed for the generalised model (discrepancies approximately 5%), even at $Ra = 10^6$. In this case, as figure 16 shows, it is due to the compensation of estimation errors (M is overpredicted by 25%, while modes L are underpredicted by 30%). At other Rayleigh numbers, the evolution of the energy of the different modes is relatively well predicted (between 5% and 20%), except for an underprediction of modes L . Overall a good agreement is observed between the different models.

The measured reorientation frequencies obtained with the coupled generalised model are given in table 11 and compared with the coupled DNS. Generally speaking, the model fairly reproduces the coupled DNS results (discrepancies of 10%–30%) and predicts the increase of the reorientation frequency with radiation, which tends to subside with the Rayleigh number. However, it should be pointed that the change in dynamics observed at $Ra = 10^6$ (loss of stability of the diagonal rolls) is not predicted with the generalised coupled model, which is consistent with the lack of validity of the modelling assumptions at this Rayleigh number.

7. Conclusion

Direct numerical simulations of RBC in a cubic cell for a radiating air–H₂O–CO₂ mixture have been performed in the Rayleigh number range $Ra \in [10^6–10^8]$. When radiative transfer is ignored (uncoupled case), the flow dynamics is always characterised by four quasi-stable diagonal states, with occasional brief reorientations between them. The stability of the diagonal states increases and the reorientation frequency decreases with the Rayleigh number in the range $3 \times 10^6 \leq Ra \leq 10^8$. When radiative transfer is taken into account (coupled case), the kinetic energy of the flow and the temperature fluctuations increase. At $Ra = 10^6$, quasi-stable planar states are observed while for $Ra \geq 3 \times 10^6$ diagonal states are retrieved. Radiation seems to increase the reorientation frequency.

A POD analysis of DNS results has been conducted and shows that the first 12 POD eigenfunctions are globally preserved over the whole Rayleigh number range,

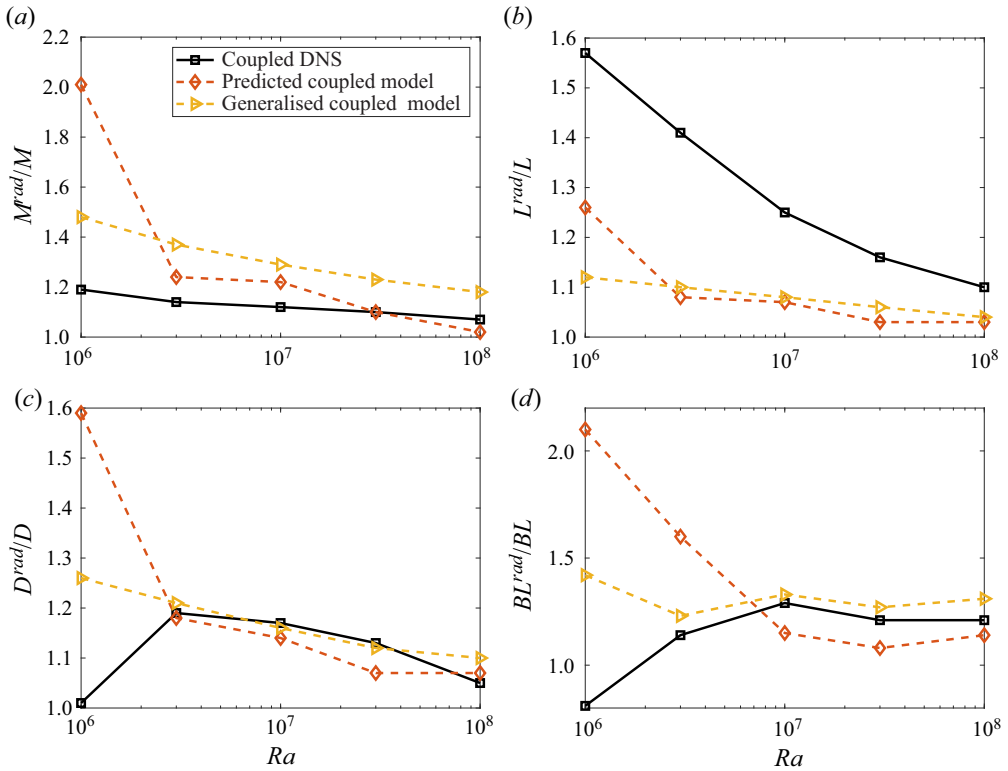


Figure 16. Relative increase of the amplitude of the large-scale modes due to radiation with the Rayleigh number – comparison of the DNS, the coupled predicted model and the coupled generalised model.

whatever the coupling conditions. However, the POD eigenvalues are higher in the coupled case at each Rayleigh number. The first seven modes identified in previous works at $Ra = 10^7$ (Soucasse *et al.* 2019, 2020) are retrieved (modes M , $L_{x/y}$, D , $BL_{x/y}$ and C), though not necessarily in the same order, depending on the Rayleigh number and the coupling conditions. Additional modes have been highlighted: (i) modes C^* , D^* , $BL_{x/y}^*$ that share common features with the previous set; (ii) modes M^* and L_z associated with toroidal and poloidal circulations and present either at low or high Rayleigh number, respectively.

Proper orthogonal decomposition-based low-order models have been derived for the uncoupled case in an *a posteriori* fashion, from uncoupled DNS data at each Rayleigh number. Truncations using either the first 12 modes or the set of key seven modes have been considered. It is shown that the set of key seven modes is sufficient to model the flow dynamics and reproduces correctly reorientation frequencies. For the coupled case, low-order models including radiation have been derived in an *a priori* fashion, solely based on uncoupled DNS data. Radiative transfer effects are linear in the model owing to the weak temperature differences. A remarkable feature of this coupled predicted model is its ability to predict the loss of stability of the diagonal states at $Ra = 10^6$. The coupled predicted model also foresees the energy increase and reorientation frequency increase associated with radiative transfer effects. Finally, a generalised model for both coupled and uncoupled cases has been proposed in order to capture variations in Rayleigh number from uncoupled DNS data at $Ra = 10^7$ and scaling laws of the uncoupled POD eigenspectrum. This generalised approach yields satisfactory results but is not able to predict the change in

dynamics at $Ra = 10^6$, even while it captures changes in energies. This shows the limit of POD model predictions when extrapolating in the range of parameters far from the original data.

In summary, this study shows that radiative transfer effects on the large-scale dynamics of RBC can be predicted satisfactorily from uncoupled simulation data over a wide range of Rayleigh number. The coupled predicted POD model derived in this paper is a valuable tool for investigating radiative transfer effects, given the high computational cost of radiation calculations. In addition, the evolution of the dynamics with the Rayleigh number can be foreseen, at least in part, from the dynamics at $Ra = 10^7$ and using scaling laws of the POD spectrum. Nevertheless, this study is restricted to the cubical geometry, given that the cavity shape alters the POD eigenfunctions and the LSC dynamics. Extension of these models to account for aspect-ratio dependencies will be the topic of future works.

Acknowledgements. This work was granted access to the HPC resources of IDRIS under the allocation 2020-A0062B00209 attributed by GENCI (Grand Equipement National de Calcul Intensif). This work was also performed using HPC resources from the ‘Mésocentre’ computing centre of CentraleSupélec and École Normale Supérieure Paris-Saclay supported by CNRS and Région Île-de-France (<http://mesocentre.centralesupelec.fr/>).

Declaration of interests. The authors report no conflict of interest.

Author ORCIDs.

 Laurent Soucasse <https://orcid.org/0000-0002-5422-8794>;

 Bérengère Podvin <https://orcid.org/0000-0001-7003-719X>.

Appendix A. Model coefficients

The low-order models for the time evolution of the POD mode amplitude $a_n(t)$, derived in §§ 4–6, all take the general form

$$\begin{aligned} \frac{da_n(t)}{dt} = & (L_{nm}^B + L_{nm}^D + L_{nm}^R)a_m(t) + Q_{nmp}a_m(t)a_p(t) \\ & + L_{nm}^A \left(1 + \frac{1}{\langle k \rangle} \sum_{p \geq 2} |a_p(t)|^2 \right) a_m(t) + \sigma \epsilon_n(t), \end{aligned} \tag{A1}$$

with $L_{nm}^R = 0$ when radiation effects are ignored. The way to determine the model coefficients is summarised in table 12 for the uncoupled model (§ 4), the predicted coupled model (§ 5) and the uncoupled and coupled generalised models (§ 6).

Coefficients L_{nm}^B , L_{nm}^D , L_{nm}^R and Q_{nmp} are, respectively, associated with buoyancy, diffusion, radiation and advection and are defined as

$$L_{nm}^B = \int Pr \phi_m^\theta \phi_n^3 \, d\mathbf{r}, \tag{A2}$$

$$L_{nm}^D = \int \left[\frac{Pr}{\sqrt{Ra}} \frac{\partial^2 \phi_m^i}{\partial x_j \partial x_j} \phi_n^i + \frac{\gamma^2}{\sqrt{Ra}} \frac{\partial^2 \phi_m^\theta}{\partial x_j \partial x_j} \phi_n^\theta \right] \, d\mathbf{r}, \tag{A3}$$

$$L_{nm}^R = \int \frac{\gamma^2}{\sqrt{Ra}} \mathcal{P}_m^{rad} \phi_n^\theta \, d\mathbf{r}, \tag{A4}$$

$$Q_{nmp} = \int \left[-\phi_p^j \frac{\partial \phi_m^i}{\partial x_j} \phi_n^i - \gamma^2 \phi_p^j \frac{\partial \phi_m^\theta}{\partial x_j} \phi_n^\theta \right] \, d\mathbf{r}, \tag{A5}$$

	Uncoupled model	Predicted coupled model	Uncoupled generalised model	Coupled generalised model
$L_{nm}^B, L_{nm}^D, L_{nm}^R, Q_{nmp}$	computed from uncoupled DNS data at each Rayleigh number ($L_{nm}^R = 0$)	computed from uncoupled DNS data at each Rayleigh number	computed from uncoupled DNS data at $Ra = 10^7 - (6.1)$ for γ ($L_{nm}^R = 0$)	computed from uncoupled DNS data at $Ra = 10^7 - (6.1)$ for γ
L_{nm}^A	determined from equilibrium relations (A6)	taken from the uncoupled model	determined from equilibrium relations (A6)p	taken from the uncoupled generalised model
a^{eq}	determined from POD spectrum	determined from equilibrium relations (A6)	determined from POD spectrum large-scale fit, (6.2)	determined from equilibrium relations (A6)
σ	computed from (4.3) using DNS POD spectrum	computed from (5.2) using equilibria a^{eq}	computed from (4.3) using fitted POD spectrum	computed from (5.2) using equilibria a^{eq}

Table 12. Model parameter determination.

Ra	10^6	3×10^6	10^7	3×10^7	10^8
σ (uncoupled model)	1.2	1.4	1.2	1.0	0.8
σ (uncoupled generalised model)	1.5	1.5	1.3	1.1	0.9
σ^{rad} (coupled predicted model)	1.9	1.5	1.2	1.0	0.8
σ^{rad} (coupled generalised model)	2.6	1.9	1.4	1.1	0.9

Table 13. Noise level $\sigma \times 10^3$ for the different models and Rayleigh numbers.

where \mathcal{P}_m^{rad} is a modal-radiative power associated with mode m , whose definition is given in Appendix B. These coefficients can be fully computed from a set of POD eigenfunctions $\{\phi^u, \gamma\phi^\theta\}$.

The adjustable coefficients L_{nm}^A can be determined from equilibria $a_n(t) = a_n^{eq}$ corresponding to a diagonal state of the flow ($da_n^{eq}/dt = 0$). Equilibrium relations write as

$$\left(L_{nm}^B + L_{nm}^D + L_{nm}^R + 2L_{nm}^A \right) a_m^{eq} + Q_{nmp} a_m^{eq} a_p^{eq} = 0. \tag{A6}$$

In the uncoupled case, equilibrium values a_n^{eq} are taken from the POD spectrum (uncoupled model) or from the large-scale fit of (6.2) (uncoupled generalised model): $a_M^{eq} = \sqrt{\lambda_M}$; $a_{Lx/y}^{eq} = \sqrt{\lambda_{Lx/y}}$; $a_D^{eq} = \sqrt{\lambda_D}$; $a_{BLx/y}^{eq} = -\eta_{BL} \sqrt{\lambda_{BLx/y}}$ and $a_n^{eq} = 0$ for the other modes. Coefficients L_{nm}^A are thus computed from (A6) with $L_{nm}^R = 0$. In the coupled case, equilibrium values are not known. However, we assume that radiation does not affect the energy transfer from the large scales to the small scales and take the adjustable coefficients from the uncoupled models. Equilibrium values with radiation can be thus predicted from equilibrium relations (A6), the adjustable coefficients being known. More details on the equilibrium value computation in the coupled case are given in Soucassee *et al.* (2020).

Finally the noise level σ is determined either from (4.3) using the POD spectrum (taken from the DNS or estimated from the fit in the generalised uncoupled model) or from (5.2) using equilibrium values in the coupled models. Noise level values are reported in table 13.

Appendix B. Computation of radiative terms

This appendix details the computation of the linear coefficients L_{nm}^R (see (A4)) associated with radiation effects in the low-order models.

Owing to the weak temperature gradients, the Planck function $I_v^\circ(T(\mathbf{r}, t))$ can be linearised around the mean temperature T_0 and the POD decomposition of the temperature field can be introduced as follows:

$$I_v^\circ(T(\mathbf{r}, t)) \simeq I_v^\circ(T_0) + \left. \frac{\partial I_v^\circ(T)}{\partial T} \right|_{T_0} \Delta T \sum_n a_n(t) \phi_n^\theta(\mathbf{r}). \tag{B1}$$

Because of the linearity of the radiative transfer equation (2.7), the radiative intensity field $I_v(\boldsymbol{\Omega}, \mathbf{r}, t)$ can be decomposed similarly,

$$I_v(\boldsymbol{\Omega}, \mathbf{r}, t) = I_v^\circ(T_0) + \left. \frac{\partial I_v^\circ(T)}{\partial T} \right|_{T_0} \Delta T \sum_n a_n(t) \psi_{v,n}^\theta(\boldsymbol{\Omega}, \mathbf{r}), \tag{B2}$$

where $\psi_{v,n}^\theta(\boldsymbol{\Omega}, \mathbf{r})$ is a modal-intensity field, associated with the POD temperature eigenfunction $\phi_n^\theta(\mathbf{r})$ and satisfying the following transport equation:

$$\boldsymbol{\Omega} \cdot \nabla \psi_{v,n}^\theta(\boldsymbol{\Omega}, \mathbf{r}) = \kappa_v (\phi_n^\theta(\mathbf{r}) - \psi_{v,n}^\theta(\boldsymbol{\Omega}, \mathbf{r})) \quad (\text{B3})$$

and boundary condition for $\boldsymbol{\Omega} \cdot \mathbf{n} > 0$,

$$\psi_{v,n}^\theta(\boldsymbol{\Omega}, \mathbf{r}^w) = \varepsilon \phi_n^\theta(\mathbf{r}^w) + \frac{1 - \varepsilon}{\pi} \int_{\boldsymbol{\Omega}' \cdot \mathbf{n} < 0} \psi_{v,n}^\theta(\boldsymbol{\Omega}', \mathbf{r}^w) |\boldsymbol{\Omega}' \cdot \mathbf{n}| d\boldsymbol{\Omega}'. \quad (\text{B4})$$

Equations ((B3)–(B4)) are solved for each POD temperature eigenfunction ϕ_n^θ using the parallel ray-tracing algorithm and the absorption distribution function model (see § 2.2 and Soucasse *et al.* (2020)). Finally, the modal-radiative power $\mathcal{P}_n^{\text{rad}}(\mathbf{r})$ in (A4) is computed according to

$$\mathcal{P}_n^{\text{rad}}(\mathbf{r}) = \frac{L^2}{\lambda} \int_v \kappa_v \left. \frac{\partial I_v^\circ(T)}{\partial T} \right|_{T_0} \left(\int_{4\pi} \psi_{v,n}^\theta(\boldsymbol{\Omega}, \mathbf{r}) d\boldsymbol{\Omega} - 4\pi \phi_n^\theta(\mathbf{r}) \right) dv. \quad (\text{B5})$$

It can be noted that the total radiative power $\mathcal{P}^{\text{rad}}(\mathbf{r}, t)$ is the sum of all modal-radiative powers, weighted by the associated POD coefficient,

$$\mathcal{P}^{\text{rad}}(\mathbf{r}, t) = \sum_n a_n(t) \mathcal{P}_n^{\text{rad}}(\mathbf{r}). \quad (\text{B6})$$

REFERENCES

- ARAUJO, F.F., GROSSMANN, S. & LOHSE, D. 2005 Wind reversals in turbulent Rayleigh–Bénard convection. *Phys. Rev. Lett.* **95**, 084502.
- BAI, K., JI, D. & BROWN, E. 2016 Ability of a low-dimensional model to predict geometry-dependent dynamics of large-scale coherent structures in turbulence. *Phys. Rev. E* **93**, 023117.
- BAILON-CUBA, J., EMRAN, M.S. & SCHUMACHER, J. 2010 Aspect ratio dependence of heat transfer and large-scale flow in turbulent convection. *J. Fluid Mech.* **655**, 152–173.
- BENZI, R. & VERZICCO, R. 2008 Numerical simulations of flow reversal in Rayleigh–Bénard convection. *Europhys. Lett.* **80**, 64008.
- BERKOOZ, G., HOLMES, P. & LUMLEY, J.L. 1993 The proper orthogonal decomposition in the analysis of turbulent flows. *Annu. Rev. Fluid Mech.* **25**, 539–575.
- BROWN, E. & AHLERS, G. 2007 Large-scale circulation model for turbulent Rayleigh–Bénard convection. *Phys. Rev. Lett.* **98**, 134501.
- BROWN, E. & AHLERS, G. 2008 Azimuthal asymmetries of the large-scale circulation in turbulent Rayleigh–Bénard convection. *Phys. Fluids* **20**, 105105.
- BROWN, E., NIKOLAENKO, A. & AHLERS, G. 2005 Reorientation of the large-scale circulation in turbulent Rayleigh–Bénard convection. *Phys. Rev. Lett.* **95**, 084503.
- CASTAING, B., GUNARATNE, G., HESLOT, F., KADANOFF, L., LIBCHABER, A., THOMAE, S., WU, X.-Z., ZALESKI, S. & ZANETTI, G. 1989 Scaling of hard thermal turbulence in Rayleigh–Bénard convection. *J. Fluid Mech.* **204**, 1–30.
- CHANDRA, M. & VERMA, M.K. 2011 Dynamics and symmetries of flow reversals in turbulent convection. *Phys. Rev. E* **83**, 067303.
- FOROOZANI, N., NIEMELA, J.J., ARMENIO, V. & SREENIVASAN, K.R. 2017 Reorientations of the large-scale flow in turbulent convection in a cube. *Phys. Rev. E* **95**, 033107.
- GIANNAKIS, D., KOLCHINSKAYA, A., KRASNOV, D. & SCHUMACHER, J. 2018 Koopman analysis of the long-term evolution in a turbulent convection cell. *J. Fluid Mech.* **847**, 735–767.
- HOLMES, P., LUMLEY, J. & BERKOOZ, G. 1996 *Turbulence, Coherent Structures, Dynamical Systems and Symmetry*. Cambridge University Press.
- JI, D. & BROWN, E. 2020 Low-dimensional model of the large-scale circulation of turbulent Rayleigh–Bénard convection in a cubic container. *Phys. Rev. Fluids* **5**, 064606.

- KOGAWA, T., OKAJIMA, J., SAKURAI, A., KOMIYA, A. & MARUYAMA, S. 2017 Influence of radiation effect on turbulent natural convection in cubic cavity at normal temperature atmospheric gas. *Intl J. Heat Mass Transfer* **104**, 456–466.
- MISHRA, P.K., DE, A.K., VERMA, M.K. & ESWARAN, V. 2011 Dynamics of reorientations and reversals of large-scale flow in Rayleigh–Bénard convection. *J. Fluid Mech.* **668**, 480–499.
- MOIN, P. & MOSER, R.D. 1989 Characteristic-eddy decomposition of turbulence in a channel. *J. Fluid Mech.* **200**, 471–509.
- NI, R., HUANG, S.-D. & XIA, K.-Q. 2015 Reversals of the large-scale circulation in quasi-2D Rayleigh–Bénard convection. *J. Fluid Mech.* **778**, R5.
- PIERROT, L., RIVIÈRE, P., SOUFIANI, A. & TAINE, J. 1999 A fictitious-gas-based absorption distribution function global model for radiative transfer in hot gases. *J. Quant. Spectrosc. Radiat. Transfer* **62**, 609–624.
- PODVIN, B. & LE QUÉRÉ, P. 2001 Low-order models for the flow in a differentially heated cavity. *Phys. Fluids* **13** (11), 3204–3214.
- PODVIN, B. & SERGENT, A. 2012 Proper orthogonal decomposition investigation of turbulent Rayleigh–Bénard convection in a rectangular cavity. *Phys. Fluids* **24**, 105106.
- PODVIN, B. & SERGENT, A. 2015 A large-scale investigation of wind reversal in a square Rayleigh–Bénard cell. *J. Fluid Mech.* **766**, 172–201.
- PODVIN, B. & SERGENT, A. 2017 Precursor for wind reversal in a square Rayleigh–Bénard cell. *Phys. Rev. E* **95**, 013112.
- PUIGJANER, D., HERRERO, J., GIRALT, F. & SIMÓ, C. 2004 Stability analysis of the flow in a cubical cavity heated from below. *Phys. Fluids* **16**, 3639.
- PUIGJANER, D., HERRERO, J., SIMÓ, C. & GIRALT, F. 2008 Bifurcation analysis of steady Rayleigh–Bénard convection in a cubical cavity with conducting sidewalls. *J. Fluid Mech.* **598**, 393–427.
- SHISHKINA, O., STEVENS, R.J.A.M., GROSSMANN, S. & LOHSE, D. 2010 Boundary layer structure in turbulent thermal convection and its consequences for the required numerical resolution. *New J. Phys.* **12**, 075022.
- SIROVICH, L. 1987 Turbulence and the dynamic of coherent structures. Part I: coherent structures. *Q. Appl. Maths* **45** (3), 561–571.
- SOUCASSE, L. 2013 Effets des transferts radiatifs sur les écoulements de convection naturelle dans une cavité différentiellement chauffée en régimes transitionnel et faiblement turbulent. PhD thesis, École Centrale Paris, France.
- SOUCASSE, L., PODVIN, B., RIVIÈRE, P. & SOUFIANI, A. 2019 Proper orthogonal decomposition analysis and modelling of large-scale flow reorientations in a cubic Rayleigh–Bénard cell. *J. Fluid Mech.* **881**, 23–50.
- SOUCASSE, L., PODVIN, B., RIVIÈRE, P. & SOUFIANI, A. 2020 Reduced-order modelling of radiative transfer effects on Rayleigh–Bénard convection in a cubic cell. *J. Fluid Mech.* **898**, A2.
- SOUCASSE, L., RIVIÈRE, P. & SOUFIANI, A. 2014a Effects of molecular gas radiation on Rayleigh–Bénard convection in a 3D cubical cavity. In *Proceedings of the 15th International Heat Transfer Conference*, pp. IHTC15–9563. Begell House.
- SOUCASSE, L., RIVIÈRE, P. & SOUFIANI, A. 2014b Subgrid-scale model for radiative transfer in turbulent participating media. *J. Comput. Phys.* **257** (Part A), 442–459.
- SOUCASSE, L., RIVIÈRE, P. & SOUFIANI, A. 2016 Natural convection in a differentially heated cubical cavity under the effects of wall and molecular gas radiation at Rayleigh numbers up to 3×10^9 . *Intl J. Heat Fluid Flow* **61-B**, 510–530.
- SOUCASSE, L., RIVIÈRE, P., XIN, S., LE QUÉRÉ, P. & SOUFIANI, A. 2012 Numerical study of coupled molecular gas radiation and natural convection in a differentially heated cubical cavity. *Comput. Therm. Sci.* **4**, 335–350.
- SOUFIANI, A. 1991 Temperature turbulence spectrum for high-temperature radiating gases. *J. Thermophys.* **5** (4), 489–494.
- SPIEGEL, E.A. 1957 The smoothing of temperature fluctuations by radiative transfer. *Astrophys. J.* **126**, 202–207.
- SREENIVASAN, K.R., BERSHADSKI, A. & NIEMELA, J.J. 2002 Mean wind and its reversal in thermal convection. *Phys. Rev. E* **65**, 056306.
- SUGIYAMA, K., NI, R., STEVENS, R.J.A.M., CHAN, T.S., ZHOU, S.-Q., XI, H.-D., SUN, C., GROSSMANN, S., XIA, K.-Q. & LOHSE, D., 2010 Flow reversals in thermally driven turbulence. *Phys. Rev. Lett.* **105**, 034503.
- VASILIEV, A., FRICK, P., KUMAR, A., STEPANOV, R., SUKHANOVSKII, A. & VERMA, M.K. 2019 Transient flows and reorientations of large-scale convection in a cubic cell. *Intl Commun. Heat Mass Transfer* **108**, 104319.

- VASILIEV, A., SUKHANOVSKII, A., FRICK, P., BUDNIKOV, A., FOMICHEV, V., BOLSHUKHIN, M. & ROMANOV, R. 2016 High Rayleigh number convection in a cubic cell with adiabatic sidewalls. *Intl J. Heat Mass Transfer* **102**, 201–212.
- VASILIEV, A.Y. & FRICK, P.G. 2011 Reversals of large-scale circulation in turbulent convection in rectangular cavities. *JETP Lett.* **93**, 330–334.
- WANG, Y., SERGENT, A., SAURY, D., LEMONNIER, D. & JOUBERT, P. 2020 Numerical study of an unsteady confined thermal plume under the influence of gas radiation. *Intl J. Therm. Sci.* **156**, 106474.
- XI, H.-D. & XIA, K.-Q. 2008 Azimuthal motion, reorientation, cessation, and reversal of the large-scale circulation in turbulent thermal convection: A comparative study in aspect ratio one and one-half geometries. *Phys. Rev. E* **78**, 036326.
- XIN, S., CHERGUI, J. & LE QUÉRÉ, P. 2008 3D spectral parallel multi-domain computing for natural convection flows. In *Parallel Computational Fluid Dynamics*, Lecture Notes in Computational Science and Engineering book Series (ed. D. Tromeur-Dervout, G. Brenner, D.R. Emerson & J. Erhel), vol. 74, pp. 163–171. Springer.
- XIN, S. & LE QUÉRÉ, P. 2002 An extended Chebyshev pseudo-spectral benchmark for the 8:1 differentially heated cavity. *Numer. Meth. Fluids* **40**, 981–998.